1   **PI 4-kinases promote cell surface expansion and facilitate tissue morphogenesis**

2   **during *Drosophila* cellularization and gastrulation**

3

4   Wei Chen, Victoria Bergstein, Bing He*

5   Department of Biological Sciences, Dartmouth College, Hanover, NH, 03755

6

7   * Correspondence to: bing.he@dartmouth.edu

8

9 **Abstract**

10   During epithelial morphogenesis, dynamic cell shape change driven by intrinsic or extrinsic forces

11   requires prompt regulation of cell surface area. Using *Drosophila* ventral furrow formation as a

12   model, we identified the PI 4-kinase Fwd as an important regulator for apical constriction-mediated

13   cell shape changes. These morphological changes involve prompt lateral surface expansion in the

14   constricting cells and apical surface expansion in the non-constricting cells adjacent to the

15   constriction domain, both of which are impeded upon depletion of Fwd. Computer modeling

16   demonstrates that restricting apical and lateral cell surface expansion will result in specific tissue-

17   level morphological abnormalities during furrow formation, which well predicts the phenotypes

18   observed in the *fwd* deficient embryos. Fwd also promotes cell surface expansion during

19   cellularization, but this function is largely redundant with another PI 4-kinase, PI4KIIα. Together,

20   our findings uncover an important role of Fwd in facilitating cell surface expansion in support of

21   dynamic epithelial remodeling.

22

Introduction

During tissue morphogenesis, cells frequently undergo dynamic shape changes in response to intrinsic or extrinsic cell-generated forces. One important task for cells during this process is to adjust their surface area to accommodate the rapid cell shape changes. Expanding surface area is particularly challenging as cell plasma membrane has low elasticity and cannot be extended by more than 3% to 5% without rupture [1]. Despite this challenge, many studies have shown that under physiological conditions, cells can manage to expand their surface area in face of the mechanical stress and still maintain membrane integrity [2–5]. The ability of cells to promptly alter their surface area under mechanical stress brings several central questions: how do cells adjust surface area while rapidly changing their shape? If active processes are involved, how do they coordinate with cell shape change? What are the consequences if cells fail to adjust surface area? Because cell shape changes are one of the fundamental cellular processes underlying tissue morphogenesis, answers to these questions are essential for understanding the mechanisms of tissue construction in development.

Ventral furrow formation during *Drosophila* gastrulation provides a good model to address those questions. The morphogenetic changes of ventral furrow formation have been well documented [6,7]. Before ventral furrow formation, embryo undergoes a special cleavage called cellularization. Cellularization begins with a syncytium with approximately 6000 nuclei aligned at the periphery of the embryo. During cellularization, plasma membrane invaginates to form cleavage furrows between the neighboring nuclei and separate them into a monolayer of epithelial cells [8]. At the end of cellularization, a group of ventrally localized mesodermal precursor cells, determined by Dorsal nuclear gradient and its downstream transcription factor Twist and Snail [9,10], undergo apical constriction and invaginate into a ventral furrow. Ventral furrow formation proceeds in two steps [7]. First, apical constriction induces a 70% increase in apical-basal cell lengthening ("lengthening

3

48   phase"). This is then followed by cell shortening and internalization as the tissue invaginates

49   ("shortening phase"). The whole process lasts about twenty minutes and results in the formation of

50   an anterior-posteriorly oriented furrow. The molecular mechanism of apical constriction has been

51   well characterized. The expression of Twist and Snail in the mesoderm precursor cells results in the

52   activation of the Fog-G protein coupled receptor (GPCR) pathway, which triggers the downstream

53   RhoA/Rho1 signaling cascade. The Rho1 signaling leads to apical assembly of F-actin and activation

54   of non-muscle myosin II (henceforth "Myosin II"), which form an actomyosin network that drives

55   apical constriction through pulsed contractions (reviewed in [11–13]).

56

57   The mechanism that mediates cell lengthening during the early phase of ventral furrow formation has

58   been recently elucidated. Quantitative analysis of 3D cell shape dynamics revealed an intimate

59   coupling between apical constriction and cell lengthening [14], which led to the proposal that

60   gastrulating cells lengthen via a purely mechanical mechanism. The cytosol acts as an

61   incompressible fluid, and constriction of apical actomyosin network generates forces that drive

62   basally directed movement of the cytoplasm, resulting in cell lengthening [14]. In line with this view, a

63   later study demonstrates that during apical constriction, the tissue interior behaves like a viscous

64   continuum and undergoes a tissue-scale laminar flow, which causes apical-basal lengthening of the

65   constricting cells [15]. Interestingly, during this process, the lateral membrane of the cells appears to

66   readily expand with the flow without impeding the flow, suggesting a close coupling between cell

67   surface expansion and the viscous movement of the cytoplasm [15]. This coupling is unlikely achieved

68   through spreading of preexisting membrane folds, as previous EM studies show no obvious

69   membrane folding prior to ventral furrow formation [16–18]. Thus, apical constriction-induced cell

70   lengthening likely involves mechanisms that add new membrane material to the cell surface.

71

72   In this study, we identified Four-wheel drive (Fwd) as an important factor regulating cell surface

4

73   expansion during the lengthening phase of ventral furrow formation. Fwd is a *Drosophila* homologue

74   of mammalian PI 4-kinase, PI4KIIIβ. Four members of PI 4-kinases have been identified in

75   mammals: PI4KIIα, PI4KIIβ, PI4KIIIα, PI4KIIIβ [19]. *Drosophila* genome encodes three PI 4-kinases

76   corresponding to the mammalian homologues except for PI4KIIβ [20]. PI 4-kinases catalyze the

77   production of PI(4)P by phosphorylation of phosphatidylinositol (PtdIns) [19,21]. Previous studies have

78   revealed various important roles for PI(4)P in regulating the endomembrane system. PI(4)P regulates

79   Golgi-to-plasma membrane transport by facilitating vesicle formation from trans-Golgi-network

80   (TGN) [22,23]. PI(4)P also serves as a recognition site for lipid transport protein such as OSBPs, FAPPs

81   and CERTs, which mediate lipid transport from ER to the Golgi [24]. Finally, PI(4)P serves as a

82   precursor for other important phosphoinositide species, such as $PI(4,5)P_2$ [25,26]. Different PI 4-kinase

83   has distinct subcellular localization and participates in different cellular processes [19,21]. PI4KIIIβ

84   localizes to TGN, where it functions partially redundant with PI4KIIα, another Golgi-localized PI4

85   kinase, in promoting antegrade trafficking from TGN [19,27]. In addition, PI4KIIIβ itself can serve as

86   scaffolding protein to recruit Rab11 to facilitate vesicle trafficking from TGN [28–30]. During

87   *Drosophila* spermatogenesis, both kinase and scaffolding activities of Fwd have been demonstrated

88   to facilitate vesicle trafficking that are important for successful meiotic cytokinesis [31].

89

90   Despite the important function of PI4KIIIβ in regulating Golgi-to-plasma membrane transport, null

91   mutant flies are viable. The only reported phenotypes in *Drosophila* are cytokinesis defect during

92   spermatogenesis and mitochondria dysfunction in neuron and muscle cells [4,31–33]. In this study, we

93   uncover a previously unappreciated role of Fwd in regulating cell surface area during early

94   embryogenesis. During ventral furrow formation, Fwd facilitates furrow invagination through its

95   separate functions in promoting cell surface expansion and regulating apical Myosin II network

96   organization. During cellularization, Fwd functions redundantly with PI4KIIα to promote cleavage

97   furrow ingression. Together, these findings demonstrated an important role for PI 4-kinases in

5

98   promoting cell surface expansion during epithelial morphogenesis.

Results

Cell surface area increases during apical constriction-mediated cell lengthening

During the lengthening phase of ventral furrow formation, cells undergoing apical constriction elongate along the apical-basal axis by a factor of ~1.7 (Figure 1A) [7]. The change of cell morphology from columnar to a more slim and elongated shape predicts a significant increase in the cell surface area (Figure 1B). To test this prediction, we imaged gastrulating embryos expressing Ecadherin-GFP and segmented individual cells in 3D following a recently described protocol [34] (Figure 1C). Consistent with the prediction, we observed an increase in both cell length and cell surface area during apical constriction (Figure 1D, E). The average rate of cell surface area increase was 28.5 μm^2/min, which resulted in an average of 26.0% ± 8.2% (mean ± s.d, n = 15 cells from 3 embryos) increase of surface area within the first 8 minutes of ventral furrow formation (Figure 1D). Accordingly, the average cell length increased by 53.0% ± 4.2% (mean ± s.d, n = 15 cells from 3 embryos) within the same time span at an average rate of 2.6 μm/min (Figure 1E). Our measurement thus confirmed that apical constriction induced cell lengthening involves a net increase of cell surface area.

Disruption of _Drosophila_ PI4KIIIβ homologue Fwd results in reduced rate of cell lengthening during apical constriction

Previous electron microscopy studies demonstrate that no obvious plasma membrane infoldings are present in the lateral membranes of the cellular blastoderm prior to gastrulation[17,18]. In addition, apical cell microvilli, which serve as a membrane reservoir for membrane ingression during cellularization, have been depleted at the end of the cellularization [16–18,35]. Therefore, it is unlikely that cell surface expansion during apical constriction is achieved through unfolding of pre-existing membrane folds. Given the non-stretchable nature of the plasma membrane [1], we hypothesized that cell lengthening/surface area increase requires membrane supply from intracellular pool of

7

124 membrane. Exocytic membrane trafficking is a tempting mechanism in this process since it has been

125 shown to promote surface area increase in many other cell shape change related processes [36].

126

127 To investigate the molecular mechanism of cell surface expansion in cells undergoing apical

128 constriction, we performed a candidate RNAi screen for genes involved in exocytic trafficking to

129 search for mutants with defective cell lengthening during ventral furrow formation (Methods; Table

130 1). For the majority of the candidates, we observed mild or no obvious cell lengthening defects and

131 embryos appeared to develop normally through early gastrulation (Table 1). This might be due to

132 either low RNAi efficiency or a non-essential function of the candidate gene during the stage of

133 interest. A subset of candidate RNAi showed severe early defects such as lack of egg laying or

134 abnormalities beyond cell lengthening defect (Arf1, Sec5, Rab11, dynein, PI4KIIIα), indicating that

135 the target genes are essential for other developmental processes earlier than gastrulation. However,

136 from this screen, we identified one interesting candidate, Fwd, the *Drosophila* homologue of

137 PI4KIIIβ that is important for the Golgi to plasma membrane trafficking. RNAi mediated maternal

138 knockdown of *fwd* resulted in reduced cell lengthening during apical constriction (Figure 2A-E). In

139 the control wildtype embryos, cell lengthening proceeded in two consecutive phases. In the first 3-4

140 minutes of apical constriction (T = 0 indicates the onset of apical constriction, same below), cell

141 length increased at an average speed of 1.6 μm/min (Figure 2B-E, cyan box). At around T = 4

142 minutes, cell lengthening speeded up and proceeded at an average speed of 2.6 μm/min (Figure 2B-

143 E, magenta box). In the *fwd* RNAi embryos, cell lengthening proceeded at an average speed of 1.7

144 μm/min during phase 1, which was comparable to the wildtype embryos. However, in phase 2, the

145 average speed in the *fwd* RNAi embryos reduced to 1.1 μm/min (Figure 2B-E). In addition, it took

146 longer time for *fwd* RNAi embryos to reach the maximum cell length. In the control embryos, cell

147 length increased from 35 μm (35.4 ± 1.5, mean ± s.d.) at the onset of apical constriction to a

148 maximum of 55 μm (55.0± 1.7, mean ± s.d.) in approximately 10 minutes. In *fwd* RNAi embryos,

149   cell length increased from 29 μm (29.3 ± 1.1, mean ± s.d.) to a maximum of 48 μm (48.2 ± 1.9, mean

150   ± s.d.) in approximately 14 minutes (Figure 2C). These results demonstrate that the rate of cell

151   lengthening during apical constriction is substantially reduced in *fwd* RNAi embryos. We observed

152   similar cell lengthening defects in embryos derived from *fwd³*/Df females [32] (Figure 2A, B),

153   suggesting that the lengthening phenotypes in the *fwd* RNAi embryos are unlikely due to off-target

154   effect of RNAi.

155

156   We noticed that the cells in *fwd* RNAi embryos at the onset of cellularization was 17% shorter than

157   that in the control embryos, suggesting that Fwd also plays a role in cell growth during

158   cellularization (Figure 2C). When we lowered the expression level of *fwd* shRNA by reducing the

159   copy number of the *GAL4* driver, the ventral cell length at the onset of apical constriction became

160   comparable to that in the wildtype embryos, yet cell lengthening during apical constriction was still

161   affected to a similar extent as in the original *fwd* knockdown embryos (Figure 2F-J). This result

162   demonstrates that the cell lengthening defects in *fwd* RNAi embryos are not due to the defect in the

163   starting cell length at the onset of gastrulation.

164

165   **Depletion of *fwd* leads to mild defects in apical constriction, but this defect cannot fully account**

166   **for the defects in cell lengthening**

167   Previous work demonstrates that apical constriction and cell lengthening are tightly coupled [14,15]. It is

168   therefore possible that the cell lengthening defects we observed in *fwd* RNAi embryos were a

169   secondary consequence of the apical constriction defects. To test this possibility, we quantified the

170   rate of apical constriction in control and *fwd* RNAi embryos by measuring the total length of the

171   apical surface of the constricting cells in the 2D cross-section view (the "apical width", red lines in

172   Figure 3A; Methods). The decrease of apical width over time was largely comparable between

173   wildtype and *fwd* RNAi embryos, except that the rate was slightly lower in *fwd* RNAi embryos

9

174 (Figure 3B, C). Thus, depletion of Fwd leads to a moderate but detectable reduction in the rate of

175 apical constriction.

176

177 Next, we asked whether the difference in apical constriction rate could account for the difference in

178 the rate of cell lengthening between wildtype and *fwd* RNAi embryos. We reasoned that if the

179 lengthening defect in *fwd* RNAi embryos was entirely caused by the reduction in the rate of apical

180 constriction, the relationship between apical constriction and cell lengthening should be the same as

181 in the control embryos. To test it, we compared the extent of cell lengthening between the two

182 genotypes when the same extent of apical constriction was achieved. In control embryos, the

183 increase in cell length was quasi-linearly related to percent apical width reduction (Figure 3D). In

184 *fwd* RNAi embryos, the increase in cell length upon the same level of apical constriction was

185 consistently lower compared to the control embryos, and the difference between the two genotypes

186 became more prominent as apical width reduction exceeds 50% (Figure 3D).

187

188 To further analyze the relationship between apical constriction and cell lengthening, we examined the

189 rate of cell lengthening during every one-minute interval as a function of the rate of apical width

190 reduction during the same time span. In the control embryos, there was a moderate positive

191 correlation between the two rates ($r^2 = 0.4$; Figure 3E). Knockdown of *fwd* resulted in reduced

192 lengthening rates compared to the control at comparable constriction rates (Figure 3E). As a result,

193 the correlation between the constriction rate and the lengthening rate became negligible for *fwd*

194 RNAi embryos ($r^2 = 0.1$; Figure 3E). In support of this observation, the ratio between cell

195 lengthening rate and constriction rate was significantly higher in wildtype embryos compared to *fwd*

196 RNAi embryos (Figure 3F, G). Together, these results indicate that although *fwd* knockdown had a

197 moderate effect on the rate of apical constriction, this effect could not fully account for the reduced

198 rate of cell lengthening in the knockdown embryos.

10

199

200 **The cell lengthening defect in *fwd* knockdown embryos is associated with defect in cell surface**

201 **expansion**

202 To determine whether the cell lengthening defect in *fwd* RNAi embryos reflects defect in cell surface

203 area increase, we performed 3D cell segmentation for the constricting cells in *fwd* RNAi embryos

204 (Figure 4A). In support of our hypothesis, we found that depletion of Fwd indeed resulted in

205 prominent defects in cell surface expansion during apical constriction, as indicated by a reduced rate

206 of cell surface area increase (control: 0-8 min: 28.5 ± 6.7 μm^2/min; *fwd* RNAi: 0-12 min: 11.6 ± 3.5

207 μm^2/min) (Figure 4B-C). As a result, the overall amount of cell surface area increase during the

208 lengthening phase was substantially reduced in *fwd* RNAi embryos (control: 208 ± 65 μm^2 over 8

209 minutes; *fwd* RNAi: 127 ± 47 μm^2 over 12 minutes) (Figure 4B-C). In addition, the increase in

210 apical-basal cell length was also reduced in *fwd* RNAi embryos, in agreement with the 2D

211 measurement (Figure 4D-E).

212

213 Of note, the cell length and cell surface area in *fwd* RNAi embryos were 19.0% and 14.5% smaller

214 than the control embryos at the onset of gastrulation (Figure 4B, D; Cell length: control: 36.1 ± 1.5

215 μm, *fwd RNAi*: 29.2 ± 1.1 μm ; Cell surface area: control: 804 ± 42 μm^2, *fwd* RNAi: 687 ± 46 μm^2),

216 consistent with the 2D measurement. In addition, the 3D analysis also confirmed the reduced rate of

217 apical constriction in *fwd* RNAi embryos (Supplementary Figure 1A). Using a similar strategy as

218 described above, we show that the difference in the rate of apical constriction could not fully account

219 for the reduced rate of cell surface expansion and cell lengthening in *fwd* knockdown embryos

220 (Figure 4F, G).

221

222 Interestingly, we noticed a difference in cell volume change between the control and *fwd* RNAi

223 embryos. In the control embryos, there was a moderate, $12\% \pm 11\%$ increase in cell volume within

11

224   the first 8 minutes of apical constriction (Supplementary Figure 1B). A small increase in cell volume

225   during the first few minutes of apical constriction has been previously reported [14]. In *fwd* RNAi

226   embryos, however, no overall volume increase was observed within the first 12 minutes of apical

227   constriction (Supplementary Figure 1B). The cause of the cell volume phenotype in *fwd* RNAi

228   embryos and its link with the cell surface area phenotype remain to be determined.

229

230   Together, our observations demonstrate that Fwd is required for proper cell surface area increase

231   during the lengthening phase of ventral furrow formation. While Fwd also plays a role in promoting

232   apical constriction, our analysis suggests that Fwd regulates cell lengthening and cell surface

233   expansion through mechanisms that are distinct from its function in apical constriction.

234

235   **Fwd regulates the coordination of apical area reduction and the spatial organization of apical**

236   **Myosin II in the constricting cells**

237   The apical constriction defects observed in *fwd* RNAi embryos prompted us to examine whether Fwd

238   also regulates cell surface area on the apical side of the cells. In addition to the mild reduction in

239   apical constriction rate, we noticed another interesting phenotype, that the apical domain of the

240   constricting cells appeared more uniform in *fwd* RNAi embryos compared to the control embryos. To

241   further analyze this phenotype, we generated the flattened surface view of the embryo (Methods) and

242   analyzed apical cell morphology at a defined stage when apical constriction reaches close to 50%

243   (Figure 5A) [37]. Specifically, we focused on the distribution of apical cell area and anisotropy across

244   the central region of the constriction domain (~6-7 cells spanning across the ventral midline, Figure

245   5B). As expected, the average cell area was similar between the two genotypes, which validated the

246   selection of stage for the analysis (Figure 5C). The average cell anisotropy was also similar between

247   the control and *fwd* RNAi embryos (Figure 5D). Despite these similarities, the constricting cells in

248   the *fwd* RNAi embryos appeared to be much more homogeneous in size and shape (Figure 5B), as

249   reflected by the significantly smaller variations in both cell area and cell anisotropy (Figure 5E, F).

250   This difference only emerged during apical constriction. Prior to gastrulation, the prospective

251   constricting cells appeared homogeneous in both wildtype and *fwd* RNAi embryos (Figure 5G-K).

252

253   Since the reduction of apical cell area during ventral furrow formation is driven by apical Myosin II

254   contractions, we next examined whether knockdown of *fwd* led to any change in apical Myosin II

255   organization during apical constriction. The apical activation and accumulation of Myosin II in *fwd*

256   RNAi embryos were comparable to wildtype control (Supplementary Figure 2, T=0-6 min), but

257   strikingly, we found that Myosin II organized into ring-like structure within the apical domain of

258   each constricting cell, in contrast to the interconnected supracellular network appearance in wildtype

259   embryos (Supplementary Figure 2, T=6-9 min). The mechanistic links between the myosin ring

260   phenotype, the reduced rate of apical constriction, and the loss of heterogeneity in apical cell shape

261   remain to be further elucidated.

262

263   **Fwd facilitates apical surface expansion in the non-constricting cells adjacent to the**

264   **constriction domain**

265   In addition to the constricting cells, depletion of Fwd also affected cell surface expansion in the non-

266   constricting cells outside of the constriction domain. During apical constriction in control embryos,

267   the apical domain of the non-constricting lateral mesodermal cells adjacent to the constriction

268   domain ("flanking cells") was pulled by the constricting cells and became stretched along the

269   mediolateral direction (Figure 6A, B). In the *fwd* RNAi embryos, however, the flanking cells

270   appeared much less stretched, and this difference, albeit less obvious, can also be seen in the more

271   laterally localized ectodermal cells (Figure 6A, A', A''). In line with these observations,

272   quantification of apical cell morphology in the non-constricting cells at 50% apical constriction

273   revealed smaller apical cell area and lower cell anisotropy in *fwd* RNAi embryos compared to the

13

274   controls (Figure 6B - D). This morphological difference was further confirmed as we compared the

275   average size of the most stretched cells at each medial-lateral row of cells (Figure 6H - J). Of note,

276   the differences in cell area and anisotropy did not exist before the onset of apical constriction (Figure

277   6E - G). Together, these observations demonstrate that the expansion of the apical domain in the non-

278   constricting cells, which is caused by mechanical stretching from the constriction domain, is

279   impaired in *fwd* RNAi embryos. The distinct phenotype in the constricting and non-constricting cells

280   raised an interesting possibility that Fwd is required for promoting cell surface expansion at both the

281   lateral and apical cell surfaces. However, the mutant phenotype manifests differently in different cell

282   groups, perhaps depending on how cells change their shape and where surface expansion is

283   triggered.

284

285   **Fwd knockdown results in slower invagination and abnormal furrow morphology**

286   Given the important role of Fwd in regulating individual cell shape during apical constriction, we

287   examined how Fwd knockdown would affect ventral furrow formation at the tissue scale. We found

288   that depletion of Fwd affected furrow invagination in various aspects (Figure 7A). First, we observed

289   a consistent difference in invagination kinetics between control and *fwd* RNAi embryos (Figure 7B).

290   In the control embryos, invagination occurred first slowly during the first ten minutes, followed by

291   an acceleration of invagination (Figure 7B). The slow and fast invagination phases corresponded to

292   the lengthening and shortening phases of ventral furrow formation, respectively (Supplementary

293   Figure 3A-B) [38]. In *fwd* RNAi embryos, the transition between the two invagination phases still

294   correlated with the transition from cell lengthening to shortening, but the lengthening phase was

295   ~46% longer compared to the control embryos (Lengthening phase duration in control: 9.4±1.4

296   minutes, mean±s.d., N=6 embryos; lengthening phase duration in *fwd RNAi*: 15.1±1.5 minutes,

297   mean±s.d., N=4 embryos; Supplementary Figure 3B). In addition, compared to the wild type, *fwd*

298   RNAi embryos displayed lower rate of furrow invagination during the shortening phase and a

14

299   moderate reduction in the final furrow depth (Figure 7B, C).

300

301   In addition to the defects in the kinetics of furrow invagination, the furrow morphology was also

302   altered in *fwd* RNAi embryos. The initial phase of ventral furrow formation was comparable between

303   the control and *fwd* RNAi embryos. However, the morphology of the furrow started to deviate

304   between control and *fwd* RNAi embryos as apical constriction progressed (Figure 7A). In both

305   genotypes, a shallow apical indentation was generated approximately 5-7 minutes after the onset of

306   apical constriction and quickly widened up to reach its maximal width. In wildtype embryos, the

307   generation of this wide apical opening was followed by a rapid narrowing of the opening as the

308   furrow folded up and invaginated. In contrast, in the *fwd* RNAi embryos, the apical indentation

309   widened to a larger extent and stayed at the wide configuration for a prolonged time (Figure 7D,

310   dashed box). Of note, the wider apical opening was not due to an expansion of the constriction

311   domain, as the number of constricting cells was comparable between the two genotypes

312   (Supplementary Figure 3C, D). The *fwd* RNAi embryos also showed morphological abnormalities at

313   the basal side of the intermediate furrow near the end of the lengthening phase. Specifically, the

314   basal side of the furrow was flatter in the *fwd* RNAi embryos compared to the control embryos at

315   equivalent invagination stages (Figure 7A, T = 07:04 in the wild type and T = 14:08 in the *fwd* RNAi

316   embryos, Figure 7E, F). Previous studies have shown that the reduction in basal myosin level is

317   important for the cells to expand their base to facilitate furrow invagination (Polyakov et al., 2014;

318   Krueger et al., 2018). We found that the extent of basal myosin loss was comparable between the

319   control and *fwd* RNAi embryos despite the difference in basal curvature, indicating that the flatter

320   base of the intermediate furrow was not caused by defects in basal myosin loss (Supplementary

321   Figure 3E). Taken together, our results demonstrate that depletion of Fwd causes specific tissue-scale

322   abnormalities in ventral furrow formation, including reduced efficiency of furrow invagination and

323   altered intermediate and final furrow morphologies.

15

324

Computer modeling suggests that restricting apical and lateral cell surface expansion may account for different aspects of the ventral furrow phenotype in *fwd* deficient embryos

In order to understand the link between the cell surface expansion defects and the tissue-level abnormalities in *fwd* RNAi embryos, we turned to a modeling approach previously developed by Polyakov et al. [38] (Figure 8A; Methods). This 2D vertex model considers the cross-section view of the embryo, where a fully invaginated furrow can be achieved through a combined action of apical constriction, elastic cell cortices ("edges" in 2D) and a non-compressible cell interior. In addition, by adiabatically reducing the basal stiffness (K_b), which mimics the gradual reduction of basal Myosin II during ventral furrow formation, the model can recapitulate different intermediate furrow morphology during the folding process [38] (Figure 8B$_1$). Finally, the ectoderm in the model undergoes moderate apicobasal thinning, a process that can occur independently of ventral furrow formation in real embryos [34]. Despite the simplifications on the morphology and mechanical properties of the cells, the model can successfully recapitulate the stepwise changes in tissue morphology during ventral furrow formation and predict the bistable characteristic of the mesoderm [34,38]. This modeling framework was advantageous in testing our hypothesis since the outcomes of the model could reveal specific morphological defects at multiple stages of furrow formation. Furthermore, the properties of the apical, basal and lateral cortices could be controlled separately in the model, thereby allowing us to examine the specific impact of restricting apical or lateral surface expansion on furrow formation.

First, we tested the impact of restricting lateral membrane expansion on ventral furrow formation. To this end, we imposed a constraint on the maximal length of the lateral edges ($l \leq l_{max}$, Methods). Under wildtype conditions, only the cells that undergo apical constriction elongate in the apical-basal direction. Therefore, only these cells would be directly impacted by the constraints on lateral expansion (Supplementary Figure 4A, magenta box). We tested conditions where l_{max} is 1.3, 1.2 or

16

349 1.1 times of the original lateral length l_0. In all three cases, the impose of the constraint on lateral

350 expansion led to a wider furrow opening and a flatter furrow base prior to the lengthening-shortening

351 transition (Figure 8B$_2$, red and blue arrows, respectively), which resembles the phenotype observed

352 in *fwd* RNAi embryos. The severity of the phenotype increases as l_{max} decreases. Despite this

353 defect, the model could still invaginate, and the final depth of the furrow was not affected (Figure

354 8B$_2$).

355

356 Using a similar approach, we next examined the impact of restricting apical membrane expansion on

357 ventral furrow formation. In this case, we imposed a constraint on the maximal length of the apical

358 edges ($a \leq a_{max}$; Methods). Under wildtype conditions, the flanking cells in the model showed most

359 prominent apical expansion, up to a factor of 2 (Supplementary Figure 4B, magenta box). In

360 addition, the more laterally localized ectodermal cells also moderately expanded their apical domain,

361 by a factor of $\sim$ 1.3 (Supplementary Figure 4B, green box). The expansion of the apical surface in

362 these cells offset the loss of apical size in the constriction domain and resulted in a $\sim$ 15% net

363 increase in the total apical surface size when the furrow was fully invaginated (Supplementary

364 Figure 4C). Interestingly, the model predicted that the impact of restricting apical expansion was

365 distinct from restricting lateral expansion. Instead of affecting the intermediate furrow morphology,

366 restricting apical expansion mainly impacted the final invagination depth. Under conditions where

367 $a_{max} >$ 1.3a_0, when the constraint mostly affected the flanking cells but not the ectodermal cells,

368 furrow invagination appeared normal (Figure 8B$_3$, $a_{max} =$ 1.4a_0; Supplementary Figure 4B, C).

369 However, under conditions where $a_{max} <$ 1.3a_0, when both the flanking cells and the ectodermal

370 cells were affected, the final invagination depth was reduced (Figure 8B$_3$; Supplementary Figure 4B,

371 C). Of note, an a_{max} of 1.25a_0 resulted in a reduction of final invagination depth from 60 μm to 50

372 μm, which is the level of defect observed in *fwd* RNAi embryos (Supplementary Figure 4C, green

373 arrow).

17

374

375   Finally, we tested the effect of combining the restrictions on apical and lateral expansion. In this

376   case, the simulated ventral furrow showed a combined phenotype, i.e., a wider furrow opening and

377   flatter base at the lengthening-shortening transition and a reduced furrow depth at the end of

378   invagination (Figure 8B$_4$). These phenotypes qualitatively resembled the morphological defects of

379   ventral furrow in *fwd* RNAi embryos, suggesting that the tissue-level abnormality in the mutant

380   embryos can be attributed to defects in cell's ability to expand its surfaces. Our model also predicts

381   that restrictions on apical and lateral surface expansion may have distinct impact on tissue-scale

382   mechanics, which would be interesting to test in the future.

383

384   **Fwd and PI4KIIα have partially redundant function in membrane growth during**

385   **cellularization**

386   Given the important function of exocytic trafficking in plasma membrane expansion, we wondered

387   whether Fwd also regulates other morphogenetic processes in early *Drosophila* embryos that require

388   cell surface expansion. As mentioned above, depletion of Fwd resulted in a moderate reduction in

389   apical-basal cell length at the beginning of gastrulation, which is indicative of cellularization defect.

390   To further analyze this phenotype, we measured cell length over time during cellularization. Previous

391   studies have shown that the ingression of cleavage furrows proceeds in separate slow and fast phases

392   during cellularization [40,41]. We found that depletion of Fwd did not significantly affect the rate of

393   furrow ingression during the slow phase, but the rate of furrow ingression during the fast phase was

394   mildly reduced compared to the control embryos (Figure 9A, B). Note that this defect was only

395   observed upon relatively strong depletion of Fwd (Figure 2F-H). The mild cellularization phenotype

396   of *fwd* RNAi embryos prompted us to ask whether other PI 4-kinases share redundant function with

397   Fwd during cellularization. Previous study has shown that another PI 4-kinase, PI4KIIα, also

398   displays Golgi localization in *Drosophila* [20]. We found that knockdown of PI4KIIα did not result in

18

399   noticeable defects in cellularization (Figure 9C, D). However, when we knocked down both Fwd and

400   PI4KIIα, the resulting embryos became severely disrupted with no sign of cellularization (Figure

401   9C). Reducing the expression level of shRNAs in the double knockdown condition prevented the

402   drastic cellularization failure but resulted in substantially reduced cell length at the end of

403   cellularization (Figure 9C, D). This dramatic additive effect suggests that Fwd and PI4KIIα function

404   in a largely redundant manner during cellularization.

405

406   Next, we asked whether functional redundancy between Fwd and PI4KIIα also exists during cell

407   lengthening in ventral furrow formation. Although PI4KIIα single knockdown did not obviously

408   affect cellularization, when these mutant embryos entered gastrulation, they showed similar defects

409   in cell lengthening as in the *fwd* deficient embryos (Figure 9E-G). Interestingly, when the double

410   knockdown embryos entered gastrulation, despite the reduced starting cell length, the rate and extent

411   of cell lengthening were comparable to those in the *fwd* single knockdown embryos (Figure 9E-G).

412   Taken together, our results revealed important function of Fwd and PI4KIIα in cell surface expansion

413   during cellularization and apical constriction-mediated cell lengthening. Interestingly, while the

414   functions of the two enzymes are largely overlapped during cellularization, their roles in cell

415   lengthening appear to be less redundant.

416

Discussion

In this study, we identified *Drosophila* PI4KIIIβ homologue, Fwd, as an important regulator of epithelial morphogenesis in early *Drosophila* embryos. During ventral furrow formation, disruption of Fwd function resulted in a reduction in the rate of cell lengthening and cell surface area increase in cells undergoing apical constriction. Depletion of Fwd also resulted in alterations in the spatial organization of apical myosin and a moderate reduction in the rate of apical constriction, but this phenotype is separable from the defects in cell lengthening and surface expansion. In addition to the constricting cells, the non-constricting cells adjacent to the constriction domain also displayed impaired surface expansion, as revealed by a reduced stretching of their apical domain compared to the wildtype embryos. Finally, during cellularization, simultaneous disruption of Fwd and another PI 4-kinase, PI4KIIα, severely affected cell surface expansion mediated by the ingression of cleavage furrows. Together, these results provide, to the best of our knowledge, the first description of the role of PI 4-kinases in promoting cell surface expansion and cell shape change during epithelial morphogenesis. Using computer modeling, we further demonstrated that restricting apical and lateral surface expansion can lead to specific defects in ventral furrow morphology that closely resemble the phenotypes observed in *fwd* deficient embryos. These findings point to a potential mechanistic link between cell surface "expandability" and tissue-scale mechanics during epithelial folding.

Previous studies have shown that Fwd plays an important role in meiotic cytokinesis during spermatogenesis [31,32,42]. In *fwd* mutant males, contractile rings can still form and constrict in dividing spermatocytes, but cleavage furrows are unstable and later retract. Fwd is known to regulate the Golgi to plasma membrane trafficking, and similar cytokinesis defects have also been observed in mutants of other Golgi associated proteins [31,42–44]. These observations suggest that the spermatocyte cytokinesis defects in *fwd* mutant are caused by defects in membrane trafficking. In this work, we showed that Fwd also contributes to membrane growth during cellularization, an atypical cytokinesis

20

442   process, although in this case Fwd functions in a largely redundant manner with PI4KIIα. Given the

443   observation that *fwd* mutants do not show obvious defects in regular mitotic cytokinesis [32], an

444   interesting future investigation is to determine the relative contribution of Golgi-localized PI 4-

445   kinases in different types of cytokinesis processes.

446

447   While numerous studies have shown the important role of exocytosis in membrane growth during

448   cytokinesis, including cellularization [45,46], the role of exocytic trafficking in cell membrane

449   expansion in support of rapid cell shape change during epithelial remodeling is less well understood.

450   We show that during ventral furrow formation, apical constriction-mediated cell lengthening

451   involves a prompt increase in the cell surface area. Our identification of Fwd, a PI4 kinase important

452   for Golgi-PM trafficking, as a regulator of cell lengthening further suggests that the observed cell

453   surface expansion involves active exocytic membrane insertion. Future experiments directly

454   monitoring new membrane addition during ventral furrow formation would be important to further

455   test this hypothesis.

456

457   So far, the only reported *fwd* phenotypes associated with surface area regulation are spermatocyte

458   cytokinesis defects initially discovered by Brill et al [32] and the cellularization and gastrulation

459   defects described in this study. A common characteristic shared between these processes is that all of

460   them involve rapid membrane expansion, which likely imposes a high demand on intracellular

461   membrane supply. In spermatocytes, meiotic divisions occur in rapid succession, causing about 60%

462   increase in surface area in less than two hours [31]. Likewise, during cellularization, the cells increase

463   their surface area 25 fold in about one hour [40,47]. During apical constriction-mediated cell

464   lengthening, the cell surface area increases by ~25% in about eight minutes. These observations raise

465   the hypothesis that the function of Fwd becomes more important when there is an acute demand for

466   membrane supply. An interesting future question is whether the activity of Fwd is subjected to

21

467   regulation by the elevated demand on intracellular membrane supply and, if so, how does the cell

468   sense such demand. Another important future question is how Fwd executes its function to facilitate

469   cell surface expansion during cellularization and cell lengthening. Two modes of PI4KIIIβ function

470   have been discovered in animal cells, both of which can promote exocytic membrane insertion.

471   PI4KIIIβ can serve as a docking site to recruit Rab11 to TGN through direct protein-protein

472   interaction, which has been observed both in vitro and in vivo [28,30]. Alternatively, PI4KIIIβ catalyzes

473   the production of PI(4)P lipids at TGN. PI(4)P helps to recruit various proteins important for

474   trafficking and can also indirectly impact trafficking through affecting other pools of membrane lipid

475   species [22–26]. Understanding the mode of action will be a key step to uncover the relevant

476   downstream molecular network regulating cell surface area during epithelial remodeling.

477

478   Our work also shed light on the impact of restricting cell surface expansion on tissue-level

479   remodeling during morphogenesis. During ventral furrow formation, disrupting the function of Fwd

480   resulted in prolonged lengthening phase, aberrant intermediate furrow morphology prior to

481   invagination, slower furrow invagination and shallower furrow at the end of invagination. While a

482   complete understanding of the cause of these phenotypes and their potential connections awaits

483   further investigation, our modeling analysis suggests that certain key aspects of the tissue-level

484   morphological abnormality in the mutant embryos can be attributed to defects in cell surface

485   expansion. It is important to note that in *fwd* deficient embryos, cell surface expansion is attenuated,

486   but not completely inhibited, which may explain the relatively moderate phenotype on ventral furrow

487   formation. Future investigations with novel approaches that allow acute and more complete block of

488   cell membrane expansion will offer a further test on this point. In addition, new modeling approaches

489   that contain the temporal components, which is lacking in our current modeling framework, will help

490   us to start to understand how restricting cell surface expansion might contribute to the defects in

491   tissue folding kinetics observed in *fwd* deficient embryos.

22

492 **Materials and methods**

493 **Fly stocks and genetics**

494 *Drosophila melanogaster* flies were grown and maintained at 18°C and crosses were maintained at

495 room temperature (21 – 23 °C). All flies were raised on standard fly food. For embryo collection,

496 flies with corresponding genotype were used to set up cages and maintained at 18°C, and embryos

497 were collected from apple juice agar plate containing fresh yeast paste.

498

499 The UAS-shRNA lines targeting *fwd* (TRiP *fwd,* BDSC stock#35257) and *PI4KIIα* (TRiP *PI4KIIα*,

500 BDSC stock#65110) were obtained from Bloomington Drosophila Stock Center. A TRiP *PI4KII*;

501 TRiP *fwd* stock were generated from cross for the double RNAi experiments. The *fwd³* mutant stock

502 (*fwd³*/TM6) was a gift from Julie Brill and have been described previously (Brill et al., 2000;

503 Polevoy et al.,2009). *fwd³* /TM6 flies were crossed to flies from a deficiency line covering the *fwd*

504 gene locus (Df(3L)Exel9057/TM6B, BDSC stock#7920) to generate loss of function *fwd* mutant.

505

506 The candidate RNAi and dominant negative lines used for the screen for lengthening defects and the

507 phenotypes in ventral furrow formation was listed in Table 1. The genes included exocytic trafficking

508 related small GTPases and their regulators and/or effectors (Rab4, Rab8, Rab11, Arf1, Sec71, Garz,

509 Nuf, Crag, Brun, Gga), motor proteins (dynein, Myosin V), lipid regulators (Cert, PI4KIIα, PI4KIIIα,

510 Fwd, Sac1) and components of exocyst complex (Sec5). For some small GTPases, the impact of

511 expression of dominant negative form of the protein was also examined [48,49].

512

513 For RNAi-mediated knockdown, female flies from RNAi lines were crossed to male flies from

514 GAL4 driver lines, and embryos from F1 flies were collected for imaging. GAL4 driver lines

515 carrying matα4-GAL-VP16 (denoted as "mat67" on the 2nd chromosome and "mat15" on the 3rd

516 chromosome) were used to drive maternal expression of shRNA in the embryo [50]. For control

517   experiment, wildtype female Oregon R flies were crossed to the GAL4 driver lines. For examining

518   the cellularization and lengthening defects, the driver line stock mat67 Sqh::mCherry; mat15

519   Ecad::GFP was used for knockdown experiments with 2 copies of GAL4, and the driver line stock

520   Sp/Cyo; mat15 Ecad::GFP was used for knockdown experiments with single copy of GAL4. Unless

521   otherwise specified, all the knockdown experiments are performed with 2 copies of GAL4.

522

523   To examine myosin in *fwd* RNAi background, female flies from Oregon R (control) and TRiP *fwd*

524   stock were crossed to male flies containing Sqh::mCherry and 2 copies of maternal GAL4 drivers.

525   Embryos from F1 flies were collected for imaging.

526

527   **Live imaging**

528   Embryos were dechorionated in 40% bleach (~3% Sodium Hydrochloride), rinsed with water 12

529   times and mounted in water with the ventral side facing up in a 35 mm MatTek glass-bottom dish

530   (MatTek Corporation). All live imaging was conducted on an upright Olympus FV-MPERS

531   multiphoton microscope equipped with the InSight Deepsee Laser System, an Olympus 25×/1.05

532   water dipping objective (XLPLN25×WMP2) and Fluoview software. 920 nm laser was used to

533   excite GFP/YFP. Unless otherwise mentioned, a 512 × 512 pixel (pixel size: 0.331 µm/pixel) of

534   region of interest was imaged using resonant scanner with frame average of 16 times. Embryos were

535   imaged from the ventral surface to 80 µm below surface with a Z step size of 1 µm and temporal

536   resolution of 53 sec/frame. For movies used for 3D reconstruction, in order to gain higher signal-to-

537   noise ratio, a 300×150pixel (pixel size: 0.331 µm/pixel) of region of interest were imaged using

538   galvanometer scanner with frame average of 4 times. The depth and step size in Z was the same

539   while the temporal resolution was set as 2 min/frame to minimize photobleaching.

540

541   **Image processing and analysis**

24

542   All images were processed using ImageJ (NIH) and MATLAB (MathWorks). Embryos were aligned

543   based on the onset of gastrulation when ventral mesodermal precursor cells start to constrict apically.

544   E-cadherin-GFP was imaged as a membrane marker for all image analyses described below.

545

546   *2D analysis of cell lengthening (cross-section view)*

547   For analysis of the rate of cell lengthening during apical constriction, an average projection of 20

548   slices of cross-section images was first generated, and the apical-basal height of the cell located at

549   the ventral midline was measured in ImageJ. For analysis of the rate of apical constriction, a row of

550   ~10 cells in mediolateral direction centered around ventral midline was selected from the en face

551   view images and tracked over time. For each time point, the farthest left and right boundary points at

552   the most apical side of this row of cells were determined and mapped onto the cross-section view

553   images. Then, the length of the apical curve between the left and right boundary points was measured

554   from the cross-section view using segmented line tool in ImageJ. To calculate the constriction rate

555   and lengthening rate, the apical domain width over time plot and cell length over time plot were first

556   smoothed and interpolated (from 2-min interval to 1-min interval), and the derivative of the resulting

557   curves were computed to determine the rate of change.

558

559   *3D analysis of cell lengthening*

560   3D segmentation and quantification of individual cells were performed as previously described [34].

561   Individual cells near the ventral midline were manually tracked over the course of ventral furrow

562   formation and segmented using the Carving tool of the "Ilastik" program [51]. For each timepoint, a Z-

563   stack of images covering the entire depth of the ventral tissue was used as the input. Manual

564   corrections were performed for the apical and basal most regions of the cells, where the automatic

565   segmentation by Ilastik was usually not optimal. Manual corrections were carried out by manually

566   outlining the cell at the relevant Z-planes using the multi-point took in ImageJ. The resulting

25

567   measurements were then incorporated into the automatic segmentation using a custom MATLAB

568   script to create the final 3D rendering of the cell. Three control embryos and three *fwd* RNAi

569   embryos were analyzed. For each embryo, 3 – 6 cells were segmented over the course of the

570   lengthening phase at 2-minute intervals.

571

572   A custom MATLAB script was used to process the reconstructed cells and analyze the cells' surface

573   area, volume, cell length along the apical-basal axis, and apical area. Surface area and volume were

574   measured using the "surfaceArea" and the "volume" functions in MATLAB, respectively. To

575   measure the apical-basal cell length and apical area, the 3D cell mask was rotated so that the cell

576   apical-basal axis became vertical. This was followed by regenerating the Z stack of 2D slices. The

577   cell length was calculated by summing up the distances between the centroids of cell slices at

578   neighboring Z-planes except for the apical-most (3 μm) and basal-most (3 μm) regions, where the

579   distances were determined by directly measuring the vertical height to avoid measurement errors due

580   to irregular shapes in these regions. The apical area was determined by measuring the average area of

581   the apical slices, ranging from 1 – 2 μm from the apical surface of the rotated cell mask.

582

583   *Analysis of apical shape and area change (surface view)*

584   For quantification of the apical cell shape, the image stack was first corrected for any tilting in the

585   mediolateral axis using ImageJ such that the ventral midline was positioned near the center of the

586   image. Next, a custom MATLAB script was used to generate a flattened surface view of the embryo

587   that accounted for the curvature of the embryo. Next, individual cell was segmented from the surface

588   view (2D) using Cellpose, a deep learning-based segmentation software [37]. A custom MATLAB

589   script was then used to extract and calculate relevant parameters such as cell position, apical area and

590   apical anisotropy. To identify the most-stretched cells from the surface view, a set of evenly spaced

591   mediolateral sampling lines were generated, and among cells falling on each sampling line, cells

26

592   with maximal area on left and right side of the ventral midline were identified as the most stretched

593   cells.

594

595   **Energy minimization-based 2D vertex model for ventral furrow formation**

596   The energy minimization-based 2D vertex model for ventral furrow formation was constructed as

597   previously described [34,38]. The model considers the cross-section view of the embryo, which contains

598   a ring of 80 columnar-shaped cells that resembles the number and geometry of the primary

599   embryonic epithelium formed during cellularization. The morphology of the cells is maintained by

600   the following mechanisms. First, the apical, basal and lateral membranes of the cells resist stretching

601   or compressing like elastic springs. Second, the cells resist changes in cell volume (area in the 2D

602   model). The model is driven out of the initial energy equilibrium by exerting the following two

603   "active" forces. First, the apex of the cells in the ventral region of the model embryo has a propensity

604   to shrink, which resembles apical constriction. Second, the apical-basal length of the ectodermal

605   cells in the model embryo has a propensity to reduce, which resembles ectodermal shortening

606   process observed in real embryos during gastrulation. Upon application of these active forces, the

607   model transitions through a series of intermediate equilibrium states by adiabatically reducing basal

608   spring stiffness, which recapitulates basal myosin loss during ventral furrow formation. These

609   intermediate equilibrium states resemble the intermediate furrow morphology observed during the

610   lengthening-shortening transition in the real embryo.

611

612   The energy equation that describes the mechanical properties of the model is given by the following

613   expression:

614
$$E = \sum_i \varphi_i \mu_i a_i^2 + \sum_i [K_l(l_i - l_0)^2 + K_b(b_i - b_0)^2 + K_a(a_i - a_0)^2]$$

615
$$+ \sum_i C_{VOL}(V_i) + C_{YOLK}(V_{yolk})$$

616 The first term in the equation describes the active apical forces that mediate apical constriction. The

617 term $\varphi_i \mu_i$ sets up the spatial distribution of apical contractility. φ_i equals to 1 for mesoderm cells (18

618 cells, with 9 cells flanking each side of the ventral midline) and 0 for the cells outside of the

619 mesoderm domain ("ectodermal cells"). μ_i is a Gaussian function that centers at the ventral midline.

620 Specifically,

621
$$\mu_i = \mu_0 e^{\frac{-(i-i_{mid})^2}{2\sigma^2}}$$

622 Here i_{mid} is the cell ID at the ventral midline, μ_0 sets up the strength of apical constriction and σ sets

623 up the width of the Gaussian function. Of note, the Gaussian function of apical force distribution in

624 the mesoderm domain is set in such a way that only 12 cells at the ventral most region of the embryo

625 will undergo apical constriction, mimicking the situation in real embryos.

626

627 The second term in the equation describes the elastic resistance of the membrane springs. a_i, b_i, and

628 l_i are the length of the apical, basal and lateral springs of cell i, respectively. The resting length of

629 these springs, a_0, b_0, and l_0, respectively, are set to be equal to the initial length of the springs. The

630 spring constant of the apical, basal and lateral springs are given by k_a, k_b and k_l, respectively. Note

631 that in order to drive apical-basal shortening of the ectoderm in the model, the resting length of the

632 lateral springs (l_0) of the cells outside of the mesoderm domain is set to be 80% of their original

633 length, as described previously [34].

634

28

635   The last two terms, C_{VOL} and C_{YOLK}, describe the constraint due to volume ("area" in 2D)

636   conservation of the cells and the yolk, respectively. When the volume deviates from the resting

637   value, penalties are imposed as described by the following equations:

638
$$C_{VOL}(V_i) = K_v(V_i - V_0)^2$$

639
$$C_{YOLK}(V_{yolk}) = K_Y(V_{yolk} - V_{0,yolk})^2$$

640   Here, V_i is the volume of cell i. V_0 is the initial equilibrium volume of cell i. Similarly, V_{yolk} is the

641   volume of the yolk. $V_{0,yolk}$ is the initial equilibrium volume of the yolk. K_v and K_{yolk} set the degree

642   of the penalty when the cell volume and the yolk volume deviate from the initial equilibrium values,

643   respectively.

644

645   The following approach is used to implement the constraint on lateral membrane expansion. When

646   the lateral spring reaches a certain threshold l_{max}, a strong penalty is implemented for any further

647   stretching of the spring. The penalty is defined as:

648
$$E_{penaltyL} = K_{pl}(l_i - l_{max})^2, when \; l_i > l_{max}$$

649   In the simulation, the following thresholds have been tested: $1.3l_0$, $1.2l_0$, and $1.1l_0$. K_{pl} is set as a

650   constant of 100,000. Note that although all cells in the model are subjected to this constraint, the

651   constraint only affected the apically constricting cells due to the way how cells change their apical-

652   basal length during ventral furrow formation.

653

654   The constraint on apical membrane expansion is implemented in a similar manner. The penalty for

655   exceeding the threshold apical spring size, a_{max}, is given by:

29

656
$$E_{penaltyA} = K_{pa}(a_i - a_{max})^2, when\ a_i > a_{max}$$

657 The thresholds for apical spring length tested in the simulation are $1.3a_0$, $1.2a_0$, and $1.1a_0$. K_{pa} is

658 set as a constant of 100,000.

659

660 List of parameters used in the simulation:

Parameter	Value
K_a	30
K_l	20
K_b *	$2^{11} \rightarrow 2^0$
μ_0	2000
σ	3
K_v	5000
K_Y	1

661

662 *: In the simulation, K_b decreases adiabatically from 2^{11} to 2^0, with a step size of 2-fold reduction.

663 Accordingly, the model transition through a series of energy-minimum equilibrium state defined by

664 each value of K_b. These equilibrium states represent the intermediate and final furrow morphology.

665

666 **Statistics**

667 Statistical comparisons were performed using two-tailed Student's t tests after Shapiro-Wilk

668 normality test. Sample sizes can be found in the figure legends.

669

30

670 **Data availability**

671 The original data generated in this work are available upon request.

672

673 **Code availability**

674 All computer codes used in this study are available upon request.

675

684

685 **Author Contributions:**

686 W.C. and B.H. designed the study. W.C. performed the experiments. W.C., V.B and B.H. analyzed

687 the data. W.C. wrote the first draft of the manuscript. All authors contributed to the final version of

688 the manuscript.

689

690 **Declaration of Interests:**

691 The authors declare no competing interests.

692

31

References

1. Morris, C. E. & Homann, U. Cell surface area regulation and membrane tension. *J. Membr. Biol.* **179**, 79–102 (2001).

2. Truschel, S. T. *et al.* Stretch-regulated exocytosis/endocytosis in bladder umbrella cells. *Mol. Biol. Cell* **13**, 830–846 (2002).

3. Aguet, F. *et al.* Membrane dynamics of dividing cells imaged by lattice light-sheet microscopy. *Mol. Biol. Cell* **27**, 3418–3435 (2016).

4. Giansanti, M. G. *et al.* Exocyst-Dependent Membrane Addition Is Required for Anaphase Cell Elongation and Cytokinesis in Drosophila. *PLoS Genet.* **11**, e1005632 (2015).

5. Tanaka, M., Fujimoto, K. & Yumura, S. Regulation of the Total Cell Surface Area in Dividing Dictyostelium Cells. *Front. Cell Dev. Biol.* **8**, 238 (2020).

6. Leptin, M. & Grunewald, B. Cell shape changes during gastrulation in Drosophila. *Development* **110**, 73–84 (1990).

7. Sweeton, D., Parks, S., Costa, M. & Wieschaus, E. Gastrulation in Drosophila: the formation of the ventral furrow and posterior midgut invaginations. *Development* **112**, 775–89 (1991).

8. Mazumdar, A. & Mazumdar, M. How one becomes many: blastoderm cellularization in Drosophila melanogaster. *Bioessays* **24**, 1012–22 (2002).

9. Leptin, M. twist and snail as positive and negative regulators during Drosophila mesoderm development. *Genes Dev* **5**, 1568–76 (1991).

10. Roth, S., Stein, D. & Nüsslein-Volhard, C. A gradient of nuclear localization of the dorsal protein determines dorsoventral pattern in the Drosophila embryo. *Cell* **59**, 1189–1202 (1989).

11. Gheisari, E., Aakhte, M. & Müller, H.-A. J. Gastrulation in Drosophila melanogaster: Genetic control, cellular basis and biomechanics. *Mech. Dev.* **163**, 103629 (2020).

12. Gilmour, D., Rembold, M. & Leptin, M. From morphogen to morphogenesis and back. *Nature* **541**, 311–320 (2017).

718   13. Martin, A. C. The Physical Mechanisms of Drosophila Gastrulation: Mesoderm and Endoderm

719   Invagination. *Genetics* **214**, 543–560 (2020).

720   14. Gelbart, M. A. *et al.* Volume conservation principle involved in cell lengthening and nucleus

721   movement during tissue morphogenesis. *Proc Natl Acad Sci U A* **109**, 19298–303 (2012).

722   15. He, B., Doubrovinski, K., Polyakov, O. & Wieschaus, E. Apical constriction drives tissue-scale

723   hydrodynamic flow to mediate cell elongation. *Nature* **508**, 392–6 (2014).

724   16. Figard, L., Xu, H., Garcia, H. G., Golding, I. & Sokac, A. M. The plasma membrane flattens out

725   to fuel cell-surface growth during Drosophila cellularization. *Dev. Cell* **27**, 648–655 (2013).

726   17. Rickoll, W. L. Cytoplasmic continuity between embryonic cells and the primitive yolk sac during

727   early gastrulation in Drosophila melanogaster. *Dev. Biol.* **49**, 304–310 (1976).

728   18. Turner, F. R. & Mahowald, A. P. Scanning electron microscopy of Drosophila melanogaster

729   embryogenesis. II. Gastrulation and segmentation. *Dev. Biol.* **57**, 403–416 (1977).

730   19. Balla, A. & Balla, T. Phosphatidylinositol 4-kinases: old enzymes with emerging functions.

731   *Trends Cell Biol.* **16**, 351–361 (2006).

732   20. Burgess, J. *et al.* Type II phosphatidylinositol 4-kinase regulates trafficking of secretory granule

733   proteins in Drosophila. *Dev. Camb. Engl.* **139**, 3040–3050 (2012).

734   21. Waugh, M. G. The Great Escape: how phosphatidylinositol 4-kinases and PI4P promote vesicle

735   exit from the Golgi (and drive cancer). *Biochem. J.* **476**, 2321–2346 (2019).

736   22. Cruz-Garcia, D. *et al.* Recruitment of arfaptins to the trans-Golgi network by PI(4)P and their

737   involvement in cargo export. *EMBO J.* **32**, 1717–1729 (2013).

738   23. Rahajeng, J. *et al.* Efficient Golgi Forward Trafficking Requires GOLPH3-Driven, PI4P-

739   Dependent Membrane Curvature. *Dev. Cell* **50**, 573-585.e5 (2019).

740   24. Mesmin, B., Kovacs, D. & D'Angelo, G. Lipid exchange and signaling at ER-Golgi contact

741   sites. *Curr. Opin. Cell Biol.* **57**, 8–15 (2019).

742   25. Dickson, E. J., Jensen, J. B. & Hille, B. Golgi and plasma membrane pools of PI(4)P contribute

33

743   to plasma membrane PI(4,5)P2 and maintenance of KCNQ2/3 ion channel current. *Proc. Natl.*

744   *Acad. Sci. U. S. A.* **111**, E2281-2290 (2014).

745   26. Thapa, N. *et al.* Phosphoinositide signaling regulates the exocyst complex and polarized integrin

746   trafficking in directionally migrating cells. *Dev. Cell* **22**, 116–130 (2012).

747   27. Minogue, S. The Many Roles of Type II Phosphatidylinositol 4-Kinases in Membrane

748   Trafficking: New Tricks for Old Dogs. *BioEssays News Rev. Mol. Cell. Dev. Biol.* **40**, (2018).

749   28. Burke, J. E. *et al.* Structures of PI4KIIIβ complexes show simultaneous recruitment of Rab11

750   and its effectors. *Science* **344**, 1035–1038 (2014).

751   29. Chalupska, D. *et al.* Phosphatidylinositol 4-kinase IIIβ (PI4KB) forms highly flexible

752   heterocomplexes that include ACBD3, 14-3-3, and Rab11 proteins. *Sci. Rep.* **9**, 567 (2019).

753   30. de Graaf, P. *et al.* Phosphatidylinositol 4-kinasebeta is critical for functional association of rab11

754   with the Golgi complex. *Mol. Biol. Cell* **15**, 2038–2047 (2004).

755   31. Polevoy, G. *et al.* Dual roles for the Drosophila PI 4-kinase four wheel drive in localizing Rab11

756   during cytokinesis. *J. Cell Biol.* **187**, 847–858 (2009).

757   32. Brill, J. A., Hime, G. R., Scharer-Schuksz, M. & Fuller, M. T. A phospholipid kinase regulates

758   actin organization and intercellular bridge formation during germline cytokinesis. *Dev. Camb.*

759   *Engl.* **127**, 3855–3864 (2000).

760   33. Terriente-Felix, A., Wilson, E. L. & Whitworth, A. J. Drosophila phosphatidylinositol-4 kinase

761   fwd promotes mitochondrial fission and can suppress Pink1/parkin phenotypes. *PLoS Genet.* **16**,

762   e1008844 (2020).

763   34. Guo, H., Swan, M. & He, B. Optogenetic inhibition of actomyosin reveals mechanical bistability

764   of the mesoderm epithelium during Drosophila mesoderm invagination. *eLife* **11**, e69082 (2022).

765   35. Figard, L. & Sokac, A. M. A membrane reservoir at the cell surface: unfolding the plasma

766   membrane to fuel cell shape change. *Bioarchitecture* **4**, 39–46 (2014).

767   36. He, B. & Guo, W. The exocyst complex in polarized exocytosis. *Curr. Opin. Cell Biol.* **21**, 537–

34

768 542 (2009).

769 37. Stringer, C., Wang, T., Michaelos, M. & Pachitariu, M. Cellpose: a generalist algorithm for

770 cellular segmentation. *Nat. Methods* **18**, 100–106 (2021).

771 38. Polyakov, O. *et al.* Passive mechanical forces control cell-shape change during Drosophila

772 ventral furrow formation. *Biophys J* **107**, 998–1010 (2014).

773 39. Krueger, D., Tardivo, P., Nguyen, C. & De Renzis, S. Downregulation of basal myosin-II is

774 required for cell shape changes and tissue invagination. *EMBO J.* **37**, (2018).

775 40. Lecuit, T. & Wieschaus, E. Polarized Insertion of New Membrane from a Cytoplasmic Reservoir

776 during Cleavage of the Drosophila Embryo. *J. Cell Biol.* **150**, 849–860 (2000).

777 41. Mahowald, A. P. Electron microscopy of the formation of the cellular blastoderm in Drosophila

778 melanogaster. *Exp. Cell Res.* **32**, 457–468 (1963).

779 42. Giansanti, M. G., Belloni, G. & Gatti, M. Rab11 is required for membrane trafficking and

780 actomyosin ring constriction in meiotic cytokinesis of Drosophila males. *Mol. Biol. Cell* **18**,

781 5034–5047 (2007).

782 43. Farkas, R. M., Giansanti, M. G., Gatti, M. & Fuller, M. T. The Drosophila Cog5 homologue is

783 required for cytokinesis, cell elongation, and assembly of specialized Golgi architecture during

784 spermatogenesis. *Mol. Biol. Cell* **14**, 190–200 (2003).

785 44. Xu, H. *et al.* Syntaxin 5 is required for cytokinesis and spermatid differentiation in Drosophila.

786 *Dev. Biol.* **251**, 294–306 (2002).

787 45. Schiel, J. A. & Prekeris, R. Membrane dynamics during cytokinesis. *Curr. Opin. Cell Biol.* **25**,

788 92–98 (2013).

789 46. Sokac, A. M., Biel, N. & De Renzis, S. Membrane-actin interactions in morphogenesis: Lessons

790 learned from Drosophila cellularization. *Semin. Cell Dev. Biol.* S1084-9521(22)00101-X (2022)

791 doi:10.1016/j.semcdb.2022.03.028.

792 47. Mazumdar, A. & Mazumdar, M. How one becomes many: Blastoderm cellularization in

793   Drosophila melanogaster. *BioEssays* **24**, 1012–1022 (2002).

794   48. Feig, L. A. Tools of the trade: use of dominant-inhibitory mutants of Ras-family GTPases. *Nat.*

795   *Cell Biol.* **1**, E25–E27 (1999).

796   49. Zhang, J. *et al.* Thirty-One Flavors of Drosophila Rab Proteins. *Genetics* **176**, 1307–1322

797   (2007).

798   50. Hunter, C. & Wieschaus, E. Regulated expression of nullo is required for the formation of

799   distinct apical and basal adherens junctions in the Drosophila blastoderm. *J Cell Biol* **150**, 391–

800   401 (2000).

801   51. Berg, S. *et al.* ilastik: interactive machine learning for (bio)image analysis. *Nat. Methods* **16**,

802   1226–1232 (2019).

803

36

804 **Table 1: Candidate RNAi and dominant negative lines used for the screen for lengthening**

805 **defects and the phenotypes in ventral furrow formation**

Gene	Inhibition method	Bloomington Stock Number	Ventral furrow formation phenotype
Rab4	RNAi	BL33757	Normal
Rab8	dominant negative	BL9780	Abnormal cell shape
Rab11	dominant negative	BL9792	No egg laying
Arf1	RNAi	BL66174, BL66175	Mild lengthening defect and abnormal cell shape
Sec71	RNAi	BL50539	Normal
Garz	RNAi	BL34987	Mild lengthening defect
Nuf	RNAi	BL44035	Normal
Crag	RNAi	BL53261	Normal
Brun	RNAi	BL64934	Normal
Gga	RNAi	BL36905, BL51170	Normal
dynein	RNAi	BL36698	No egg laying
dynein	RNAi	BL36583	Mild lengthening defects
MyosinV	RNAi	BL55174	Normal
Cert	RNAi	BL35579, BL60080	Mild lengthening defect
PI4KIIα	RNAi	BL35278, BL65110	Mild lengthening defects
PI4KIIIα	RNAi	BL35643	No egg laying
Fwd	RNAi	BL35257	Lengthening defects
Sac1	RNAi	BL56013	Normal
Sec5	RNAi	BL50556	Mild lengthening defect and abnormal cell shape

806

807 Note: Phenotypes were assessed based on visual inspection.

37

808   **Figures and Figure Legends**

809   # Figure 1
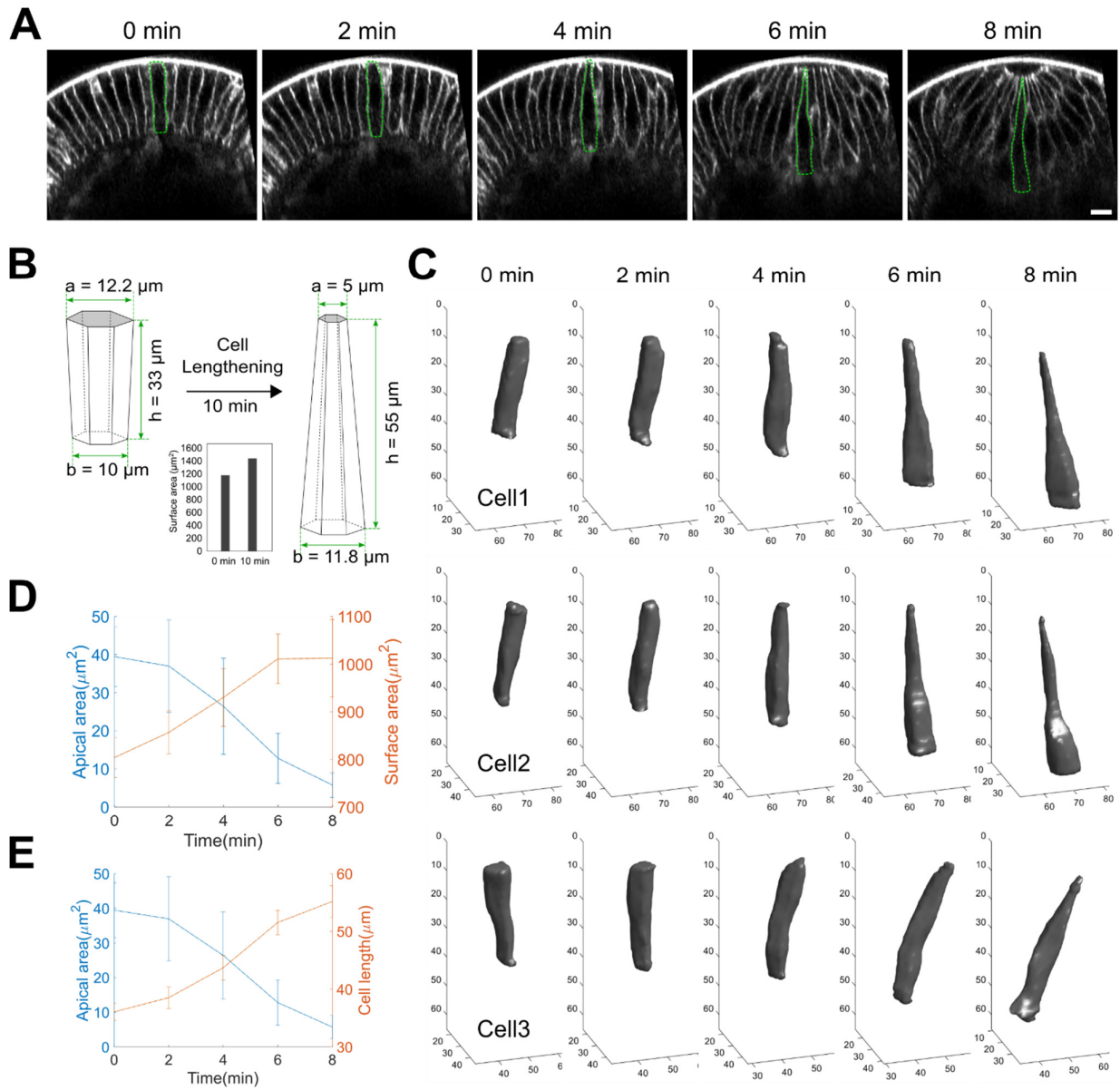
811 **Figure 1. Cell surface expands during apical constriction induced cell lengthening.**

812 **(A)** Cross-section view of an embryo expressing E-cadherin-GFP showing ventral furrow formation.

813 Ventral side is up. For each frame, the outline of a single cell is shown as an example. Scale bar: 10

814 μm.

815 **(B)** Predicted cell surface area increase based on the observed cell shape change in the constriction

816 domain.

817 **(C)** Examples of three-dimensional reconstruction of ventral cells from a wildtype embryo during

818 apical constriction.

819 **(D, E)** Apical area and cell length (D) or cell surface area (E) over time during apical constriction.

820 N=15 cells from 3 embryos. Error bars stand for s.d.

821

822 **Figure 2**

823

40
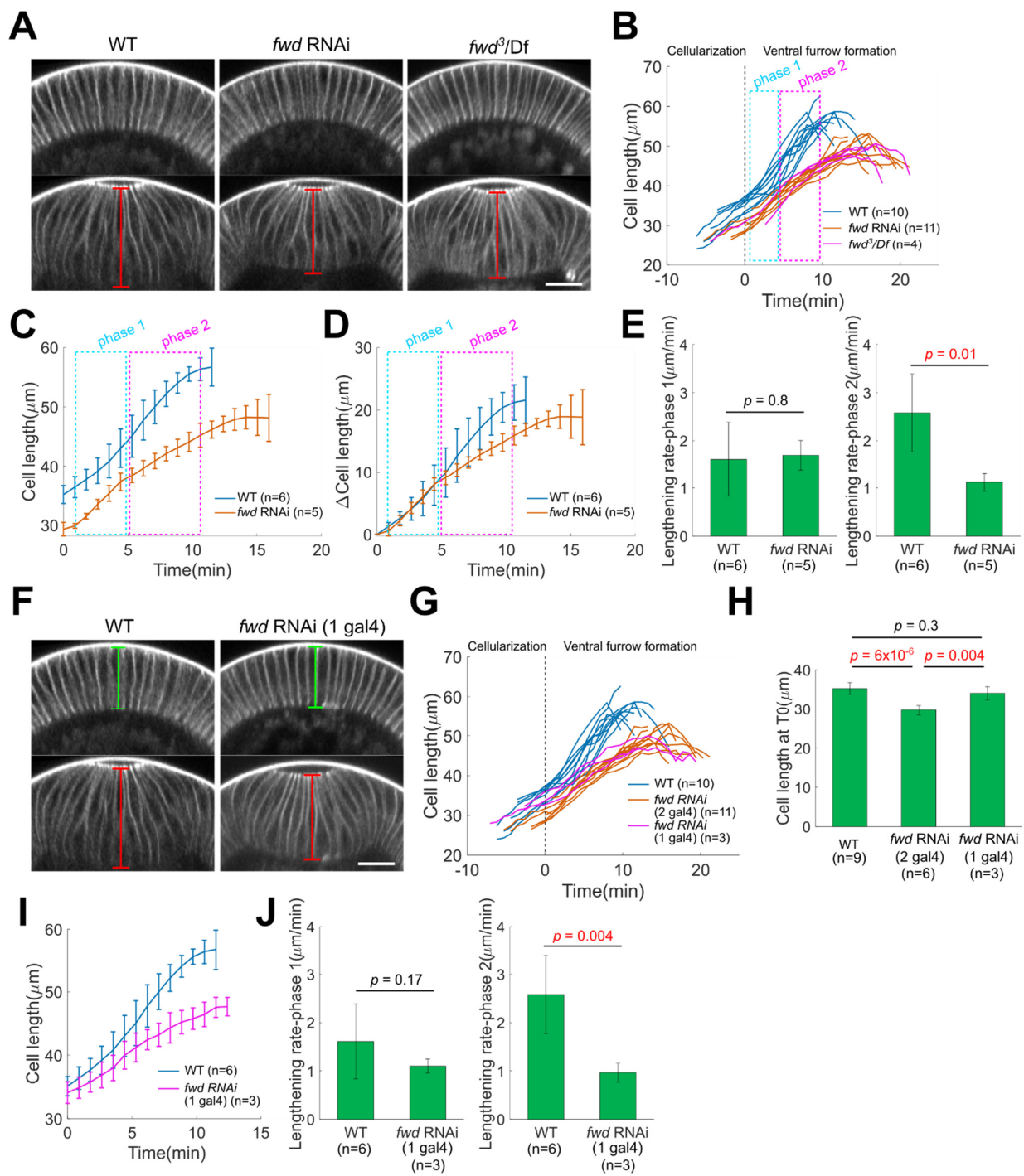
824   **Figure 2. Fwd knockdown results in cell lengthening defect during ventral furrow formation.**

825   **(A)** Representative cross-section views showing wildtype, *fwd* RNAi and *fwd* loss of function mutant

826   embryos at the onset of ventral furrow formation (top) and near lengthening-shortening transition

827   (bottom). Apical-basal length of the constricting cell at the center of the furrow (red lines) was

828   measured over time. Scale bar, 20 μm.

829   **(B)** Cell length over time for different genotypes. In wildtype embryos, cell lengthening proceeds in

830   two phases with distinct rates (cyan and magenta boxes). *fwd* loss of function mutants and *fwd* RNAi

831   embryos exhibit similar lengthening defect. 0 min is defined as the onset of apical constriction

832   throughout the text.

833   **(C, D)** Average cell length over time before (C) or after (D) subtracting the cell length at 0 min. Error

834   bars stand for s.d..

835   **(E)** Rate of cell lengthening at phase 1 and phase 2. Error bar stands for s.d..

836   **(F)** Representative cross-section views showing wildtype embryo and *fwd* RNAi embryo with one

837   copy of Gal4. Top: onset of ventral furrow formation. Bottom: near the lengthening-shortening

838   transition. Green and red lines indicate cell length at different stages. Scale bar, 20 μm.

839   **(G)** Cell length change over time. For G and H, Data for WT and *fwd* RNAi (2 gal4) are reused from

840   (B).

841   **(H)** Cell length at the end of cellularization. Error bar stands for s.d.. For H – J, Data for WT are
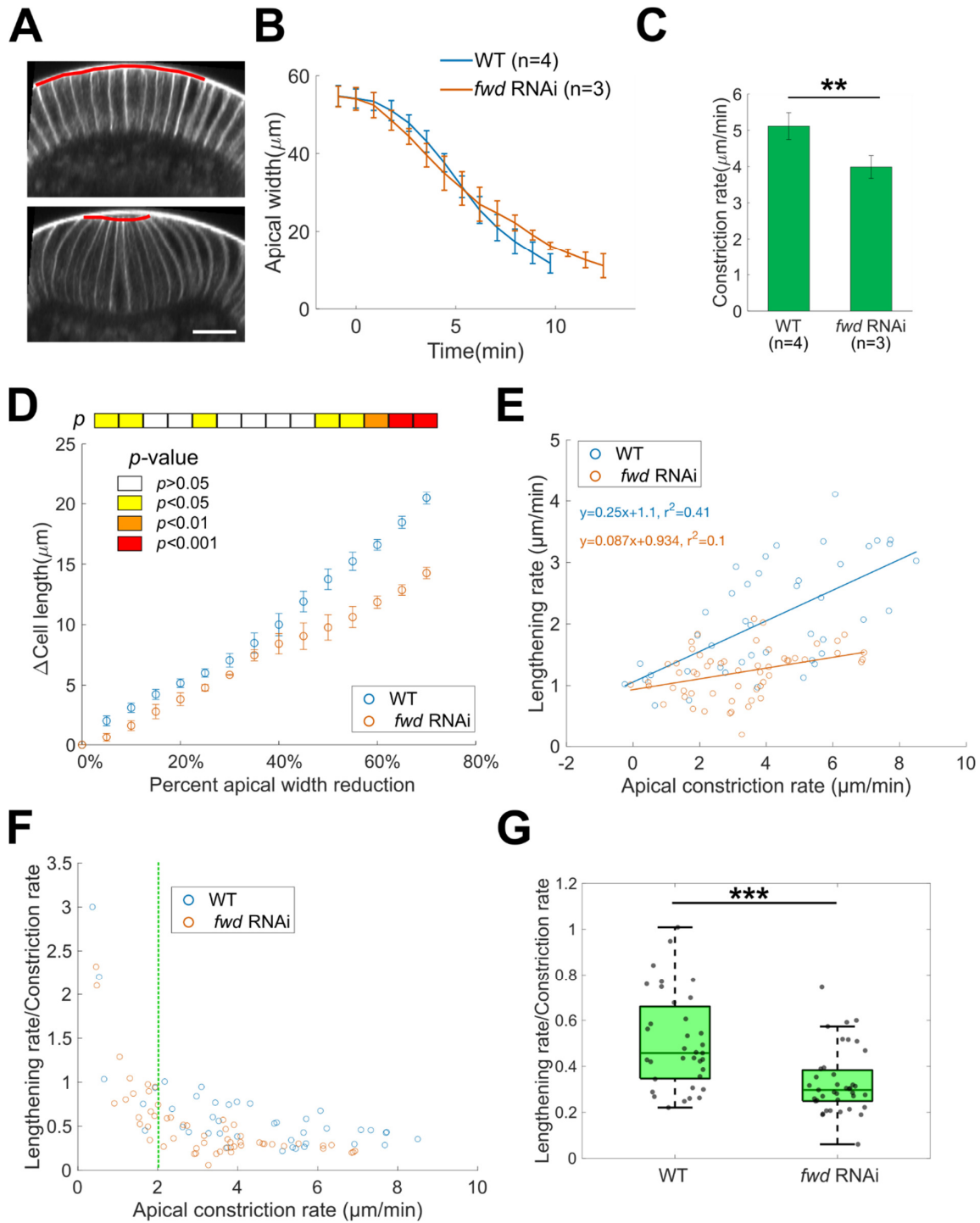
842   reused from (B).

843   **(I)** Average cell length over time. Error bars stand for s.d..

844   **(J)** Rate of cell lengthening at phase 1 and phase 2. Error bar stands for s.d..

845   Two tailed, unpaired Student's t test is used for all statistical analysis shown in this figure.

846

847 **Figure 3**

850 **Figure 3. Knockdown of *fwd* leads to mild defects in apical constriction, but this defect cannot**

851 **fully account for the defects in cell lengthening**

852 **(A)** Example showing the measurement of apical constriction domain width from the cross-section

853 views (red lines). A row of ~10 cells centering around ventral midline were measured over time

854 (Methods).

855 **(B)** Average apical constriction domain width over time. Error bars stand for s.d..

856 **(C)** Constriction rate during 3 – 10 min. **: $p < 0.01$. Two tailed, unpaired Student's t test.

857 **(D)** Cell length increase as a function of percentage apical area reduction. With the same degree of

858 apical constriction, *fwd* RNAi embryos show less cell lengthening compared to wildtype embryos.

859 Error bars stand for s.e.m.. p-values are shown as a color bar on the top of the plot. Two tailed,

860 unpaired Student's t test.

861 **(E)** Scatter plot of cell lengthening rate as a function of constriction rate.

862 **(F)** Scatter plot of the ratio between cell lengthening rate and apical constriction rate as a function of

863 apical constriction rate. For the analysis shown in (G), data points with constriction rate smaller than

864 2 μm/min (green dotted line) were excluded.

865 **(G)** Comparison of the cell lengthening rate/apical constriction rate ratio between wildtype and *fwd*

866 RNAi embryos. ***: $p < 0.001$. Two tailed, unpaired Student's t test.

867

868 **Figure 4**

869

44
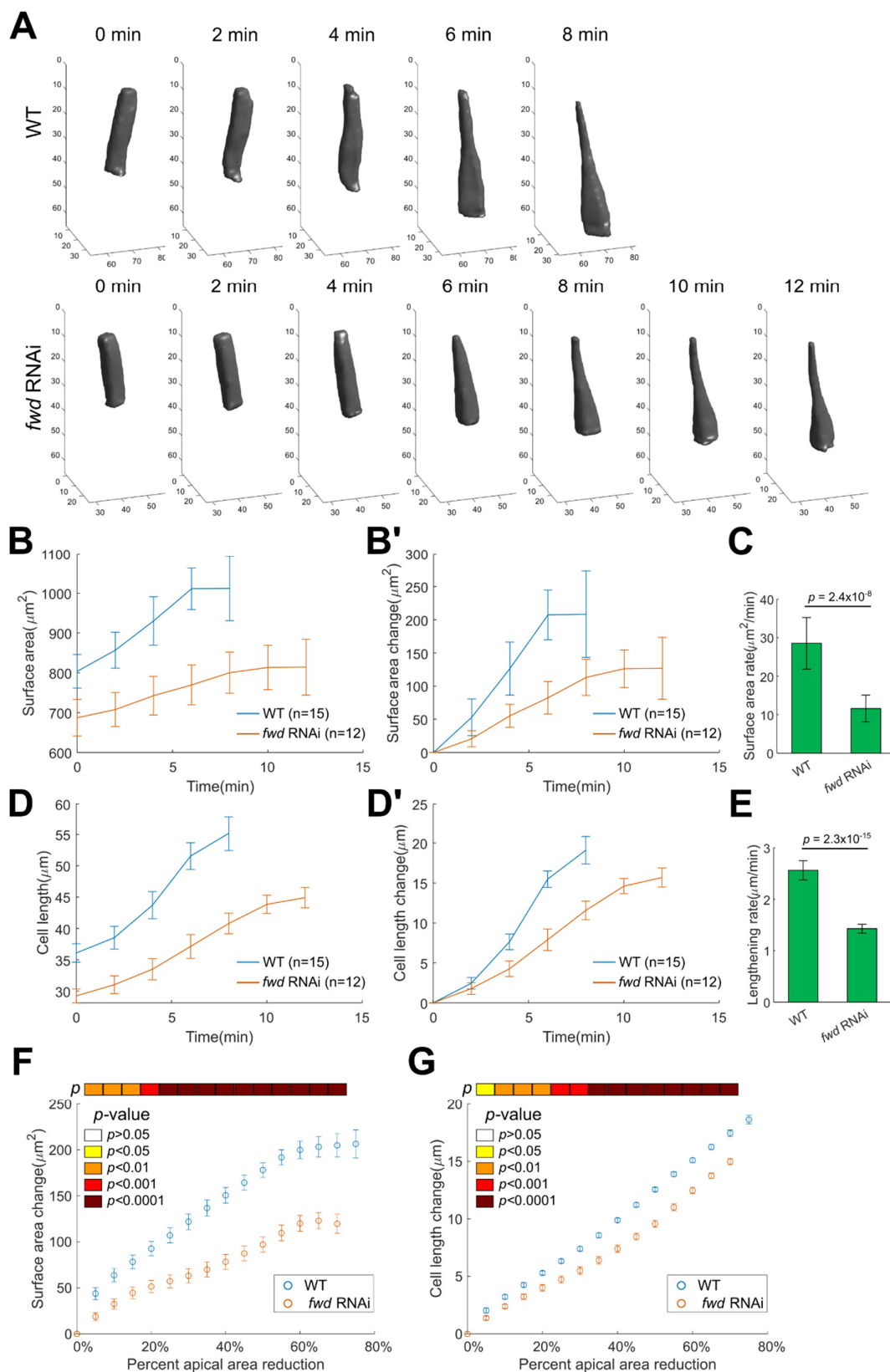
870   **Figure 4. Cell lengthening defect in *fwd* RNAi embryos is associated with reduced cell surface**

871   **expansion.**

872   **(A)** Representative three-dimensional reconstruction of ventral cells undergoing apical constriction

873   in wildtype and *fwd* RNAi embryos. Image sequence begins at the onset of gastrulation and ends ∼ 2

874   min before lengthening-shortening transition. The wildtype data shown in Figure 1 were reused in

875   this figure for comparison.

876   **(B, B')** Average cell surface area over time before (B) or after (B') subtracting the value at 0 min.

877   For wildtype, N=15 cells from 3 embryos; For *fwd* RNAi, N=12 cells from 3 embryos (same below).

878   Error bars stand for s.d..

879   **(C)** Rate of the surface area change during the lengthening phase. Error bars stand for s.d..

880   **(D, D')** Average cell length over time before (D) or after (D') subtracting the value at 0 min. Error

881   bars stand for s.d..

882   **(E)** Rate of the cell length change during the lengthening phase. Error bars stand for s.d..

883   **(F, G)** Cell surface area increase (F) and cell length increase (G) measured from 3D reconstructed

884   cells as a function of the percentage decrease of apical area. The percentage decrease of apical area

885   was measured by averaging the apical area of 80 wildtype and 72 *fwd* RNAi cells located at the mid-

886   ventral region of the embryo (from 3 wildtype and 3 *fwd* RNAi embryos, respectively). Error bars

887   stand for s.e.m.. p-values are shown as a color bar on the top of the plot.

888   Two tailed, unpaired Student's t test is used for all statistical analysis in this figure.

889

45
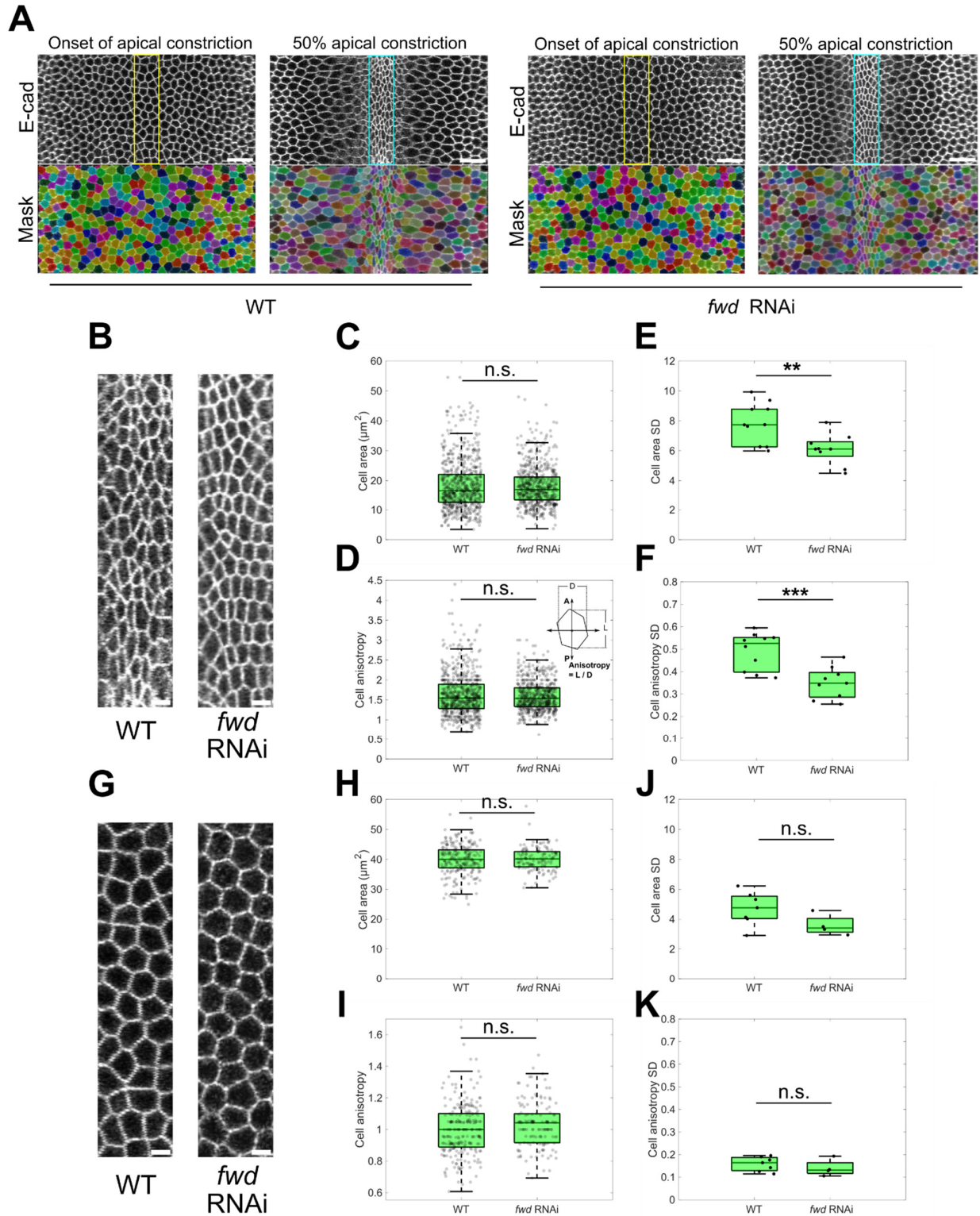
Figure 5

892 **Figure 5. Depletion of Fwd results in more uniform cell shape in the constriction domain.**

893 **(A)** Cell segmentation at the ventral surface of the wildtype and *fwd* RNAi embryos at the onset of

894 apical constriction and when apical area of the constriction domain reduces to ~ 50%. Cyan and

895 yellow boxes mark cells located at the middle of the constriction domain that were typically used for

896 analysis in B – F and G – K, respectively. Scale bars, 20 μm.

897 **(B)** Zoom-in view of cells inside cyan box in (A). Scale bars, 5 μm.

898 **(C-D)** Cell area (C) and anisotropy (D) of individual constricting cells at ~ 50% apical area

899 reduction. 723 constricting cells from 10 wildtype embryos and 648 constricting cells from 9 *fwd*

900 RNAi embryos were plotted. n.s.: not significant. Two tailed, unpaired Student's t test.

901 **(E-F)** Standard deviation of cell area (E) and cell anisotropy (F) for constricting cells. Same cells as

902 in C and D were plotted. **: $p < 0.01$; ***: $p < 0.001$. Two tailed, unpaired Student's t test.

903 **(G)** Zoom-in view of cells inside yellow box in (A). Scale bars, 5 μm.

904 **(H-I)** Cell area (H) and anisotropy (I) of individual cells in the middle of the constriction domain at

905 the onset of apical constriction. 242 constricting cells from 7 wildtype embryos and 139 constricting

906 cells from 4 *fwd* RNAi embryos were plotted. n.s.: not significant. Two tailed, unpaired Student's t

907 test.

908 **(J-K)** Standard deviation of cell area (J) and cell anisotropy (K) for constricting cells. Same cells as

909 in H and I were plotted. n.s.: not significant. Two tailed, unpaired Student's t test.

910

47

911 **Figure 6**
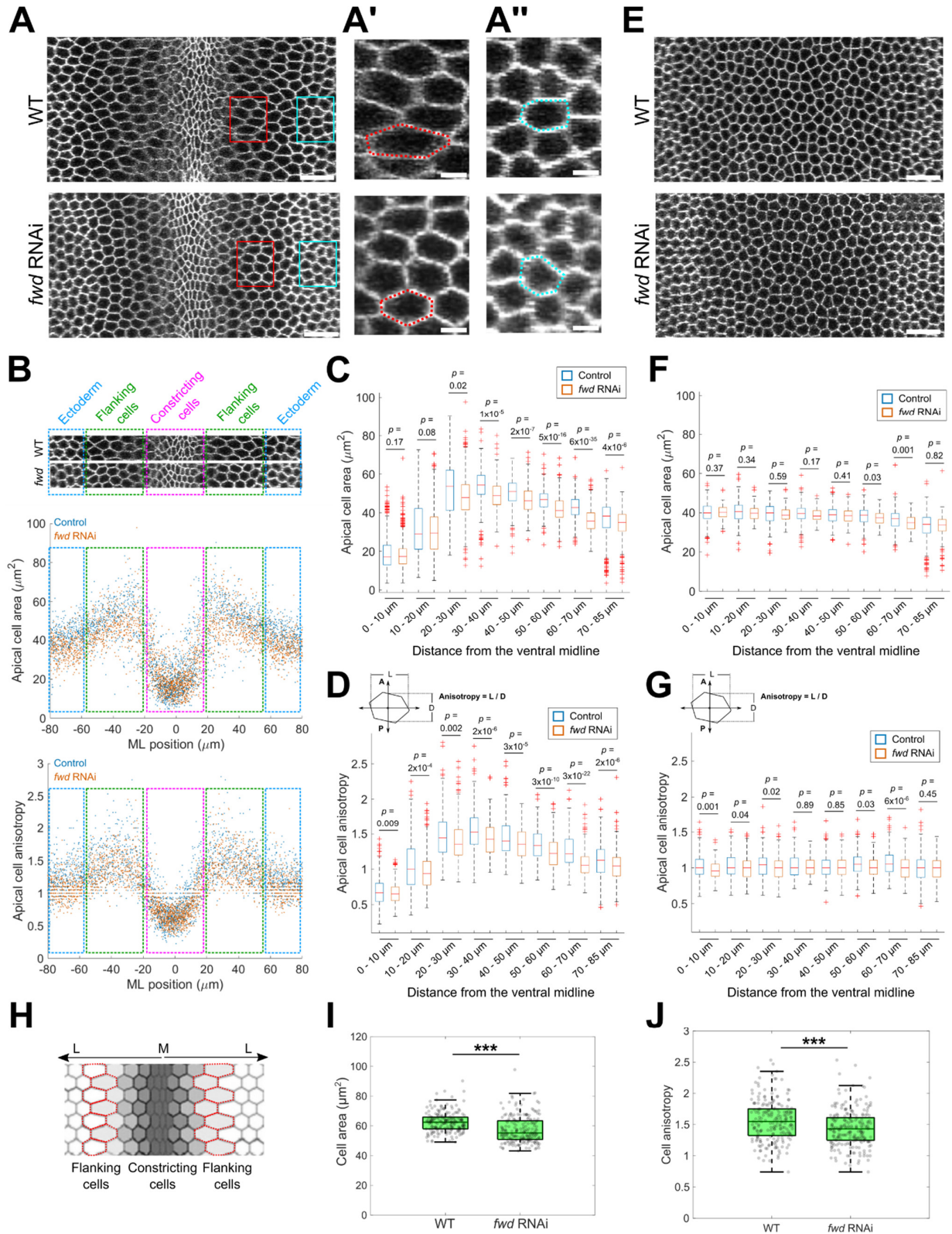
912

913 **Figure 6. Flanking cells are less stretched in *fwd* RNAi embryos than in the control embryos**

914 **when similar degree of apical constriction is achieved.**

915 **(A)** Surface view of wildtype and *fwd* RNAi embryos when apical area of the constriction domain

916 reduces to ~ 50%. Scale bars, 20 μm. (A') and (A'') are the zoom-in view of the flanking cell region

917 and the lateral ectoderm region marked by the red box and cyan box in (A), respectively. Red and

918 cyan dotted lines show examples of one cell in each genotype. Scale bars, 5 μm.

919 **(B)** Cell area (top) and cell anisotropy (bottom) distribution along mediolateral direction at 50%

920 apical constriction. 0 μm marks the ventral midline. Different regions are indicated with colored

921 boxes. Cells from 9 wildtype and 9 *fwd* RNAi embryos were pooled together.

922 **(C, D)** Comparison of cell area (C) and anisotropy (D) between wildtype and *fwd* RNAi embryos at

923 50% apical constriction for cells located at different distance from the ventral midline. Two tailed,

924 unpaired Student's t test.

925 **(E)** Surface view of wildtype and *fwd* RNAi embryos before apical constriction. Scale bars, 20 μm.

926 **(F, G)** Comparison of cell area (F) and anisotropy (G) between wildtype and *fwd* RNAi embryos

927 before apical constriction. Cells from 7 wildtype and 4 *fwd* RNAi embryos were pooled together.

928 Two tailed, unpaired Student's t test.

929 **(H-J)** Apical area and anisotropy of the most stretched cells along the mediolateral at 50% apical

930 constriction. (H) The most stretched cells in each row of cells (red outlines) that are quantified in (I)

931 and (J). (I) Apical cell area. (J) Apical cell anisotropy. Wildtype: N=203 cells from 9 embryos; *fwd*

932 RNAi: N=210 cells from 9 embryos. ***: $p < 0.001$. Two tailed, unpaired Student's t test.

933

934 **Figure 7**
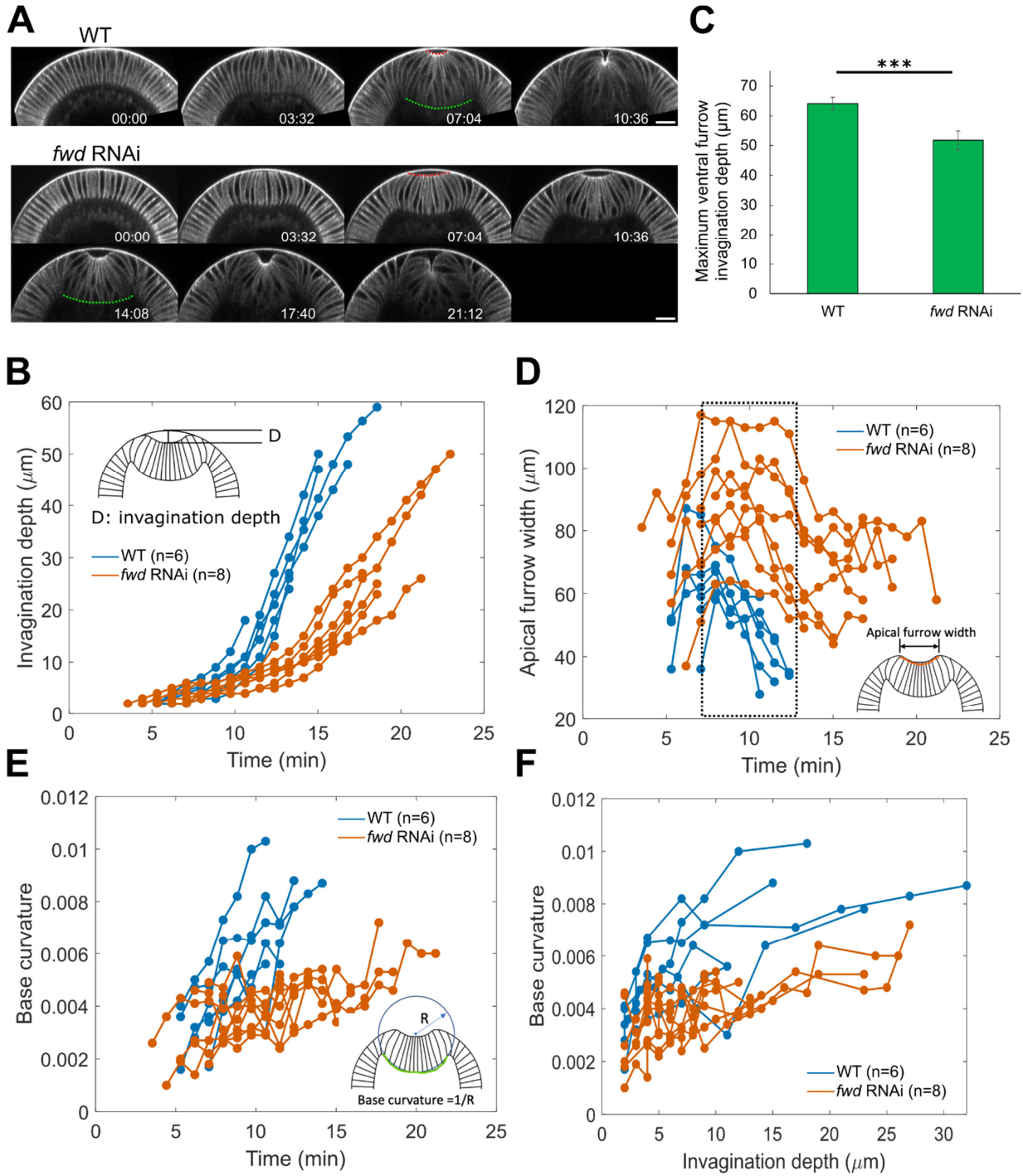
935

936 **Figure 7. Depletion of Fwd results in slower ventral furrow invagination and abnormal furrow**

937 **morphology.**

938 **(A)** Representative movie stills showing the cross-section view of ventral furrow for wildtype and

939 *fwd* RNAi embryos. Scale bars, 20μm.

940 **(B)** Invagination depth over time. For all the quantifications in this figure, N=6 embryos for

941 wildtype, N=8 embryos for *fwd* RNAi embryos unless otherwise mentioned.

942 **(C)** Maximum invagination depth. N=4 embryos for both wildtype and *fwd* RNAi embryos. Error

943 bars stand for s.d., ***: p < 0.001. Two tailed, unpaired Student's t test.

944 **(D)** Apical furrow width over time. Dashed box indicates a prolonged phase with wide open furrow

945 in *fwd* RNAi embryos.

946 **(E)** Furrow base curvature over time.

947 **(F)** Furrow base curvature as a function of invagination depth. Furrow base curvature is higher in the

948 control embryos than in *fwd* RNAi embryos at comparable invagination depth.

949

51

950 **Figure 8**
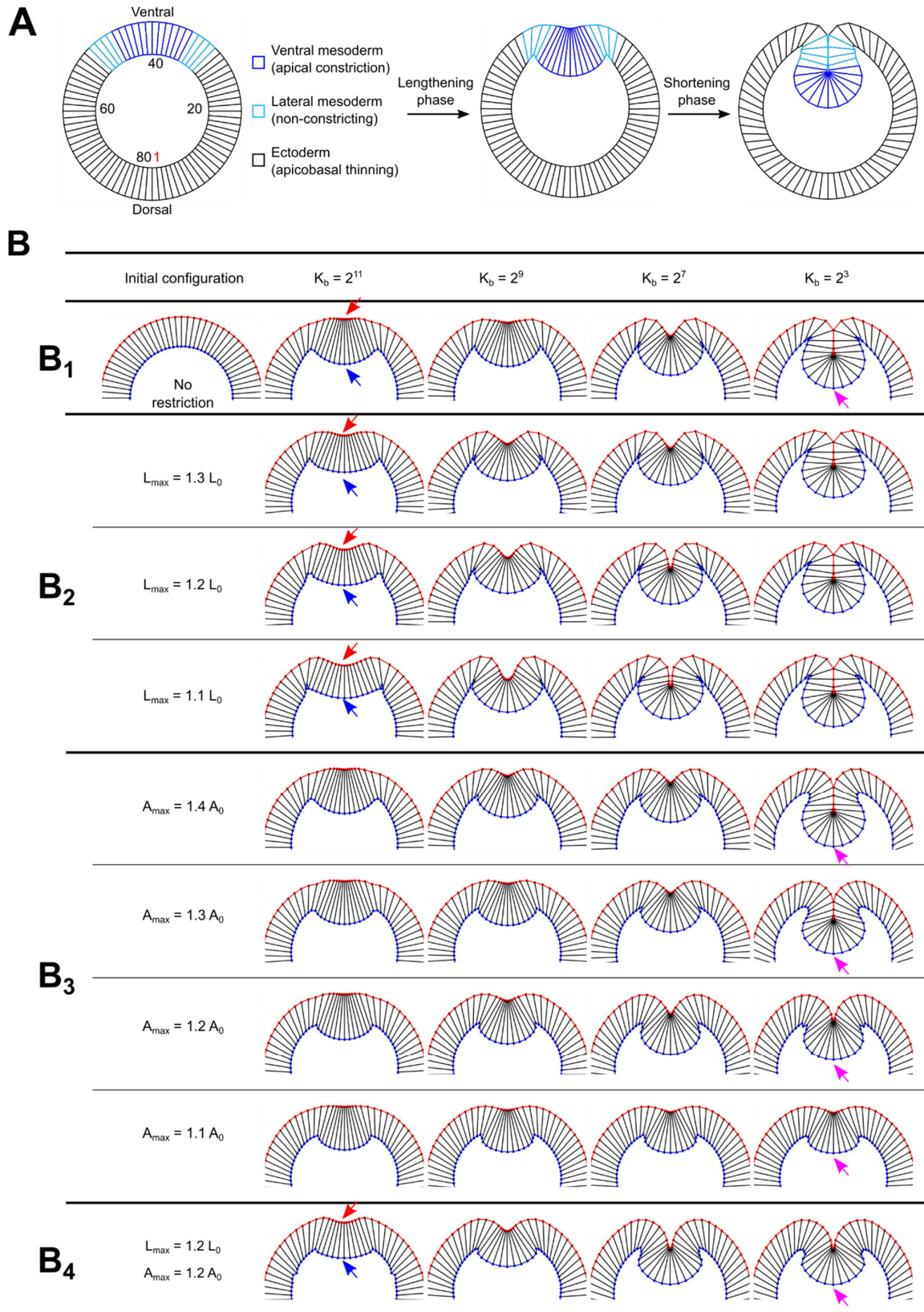
951

952 **Figure 8. Simulation shows distinct impact of restricting apical and lateral surface expansion**

953 **on ventral furrow formation.**

954 **(A)** 2D vertex model testing the impact of defects in cell surface expansion on ventral furrow

955 formation. The model considers the cross-section view of the embryo, which contains a ring of 80

956 columnar-shaped cells. In the model, the cortices of cells resist deformations as elastic springs, and

957 the cells have a strong propensity to maintain constant volume. The model is driven out of

958 equilibrium by apical constriction in the ventral mesoderm (the upmost 12 cells). In addition, the

959 ectodermal cells located outside of the mesoderm domain undergo apical-basal shortening of the

960 ectoderm (Methods).

961 **(B)** Simulation results ($B_1 - B_4$).

962 **(B_1)** When simulating normal ventral furrow formation, the model transitions through a series of

963 equilibrium states governed by a stepwise reduction of basal stiffness (K_b).

964 **(B_2)** Ventral furrow formation when the maximal elongation of the lateral membrane (L_{max}) is

965 constrained to 1.3-, 1.2- and 1.1-fold of its original length L_0. As the constraint on L_{max} increases, the

966 morphology of the intermediate furrow becomes increasingly abnormal, featured by a wider apical

967 indentation (red arrows) and a flatter base (blue arrows). On the other hand, the final invagination

968 depth is not affected.

969 **(B_3)** Ventral furrow formation when the maximal elongation of the apical membrane (A_{max}) is

970 constrained to 1.4-, 1.3-, 1.2- and 1.1-fold of its original length A_0. As the constraint on A_{max}

971 increases, the final furrow depth becomes increasingly smaller (magenta arrows). The intermediate

972 furrow morphology is not substantially affected.

973 **(B_4)** When both L_{max} and A_{max} are constrained to 1.2-fold of their original length, the effects are

974 additive, and the model shows defects in both intermediate furrow morphology and the final

975 invagination depth, which recapitulate the ventral phenotype in *fwd* deficient embryos.

976

977 **Figure 9**

54
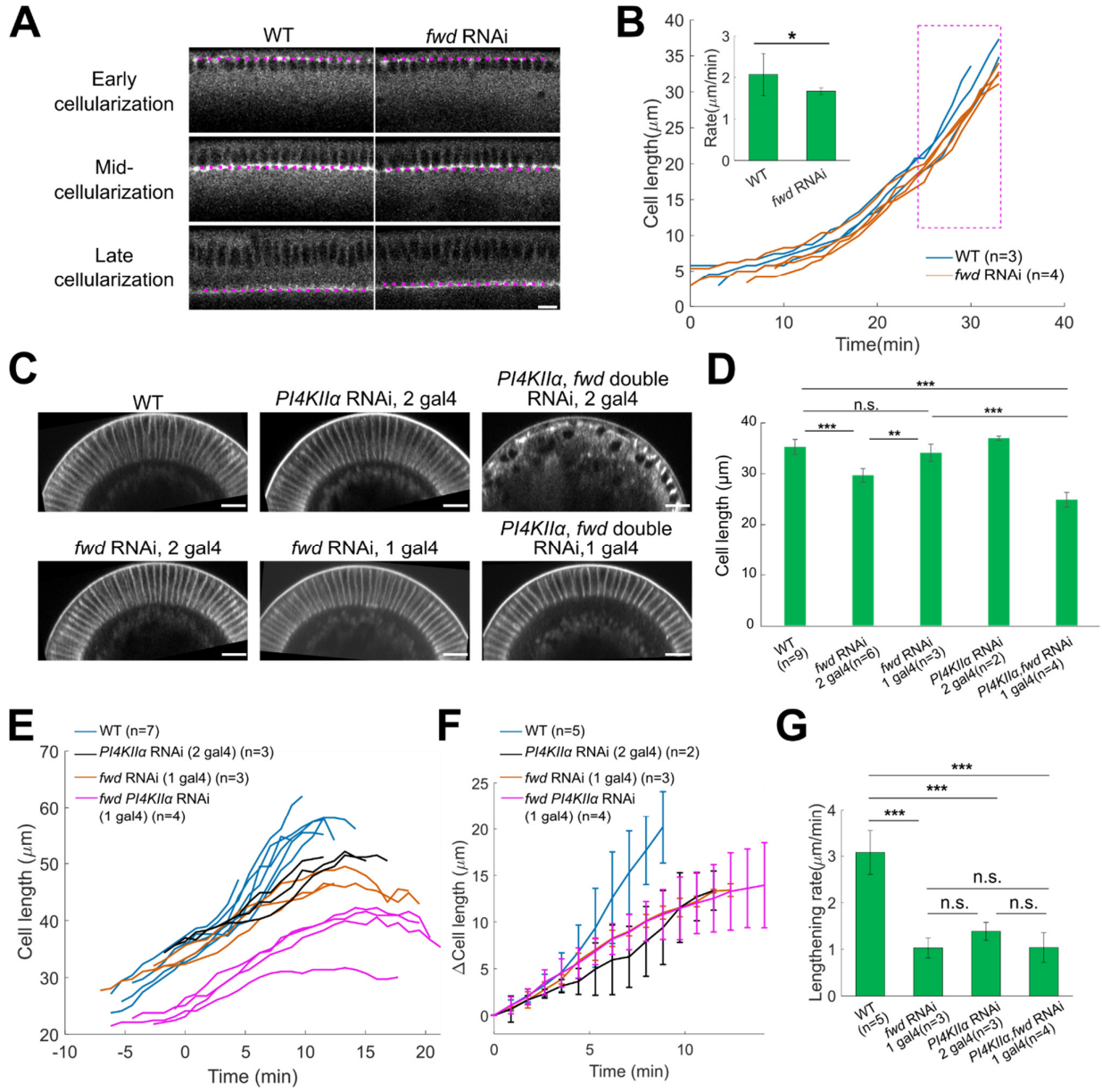
979 **Figure 9. Fwd and PI4KIIα function redundantly in cell membrane growth during**

980 **cellularization**

981 **(A)** Membrane growth during cellularization in wildtype and *fwd RNAi* embryos. Midsagittal plane

982 images at the dorsal side of the embryo were taken over time. Cellularization front (magenta dotted

983 lines) was visualized by Sqh-mCherry. Scale bar, 10 μm.

984 **(B)** Cell length over time during cellularization. Time 0 is the time point when the cellularization

985 front reaches the top of the nuclear. For embryos missing time 0, embryos are aligned based on the

986 general trend of cleavage furrow ingression. Inset shows the rate of furrow ingression during late

987 cellularization (magenta box). Error bar stands for s.d.; *: $p < 0.05$; One-sided Wilcoxon rank sum

988 test.

989 **(C)** Representative cross-section view images of embryos from different genetic background at the

990 end of cellularization. Scale bars, 20 μm.

991 **(D)** Quantification of cell length at the end of cellularization for different genetic background. Error

992 bar stands for s.d.; n.s.: not significant; ***: $p < 0.001$; **: $p < 0.01$; Two tailed, unpaired Student's t

993 test.

994 **(E)** The length of the apically constricting cells over time during apical constriction for embryos

995 from the indicated genetic backgrounds. 0 min represents the onset of gastrulation.

996 **(F)** Average length of the apically constricting cells over time during apical constriction. Error bar

997 stands for s.d..

998 **(G)** Rate of cell lengthening at phase 2. Error bar stands for s.d.. n.s.: not significant; ***: $p < 0.001$;

999 Two tailed, unpaired Student's t test.

1000